Utrecht University

MASTER THESIS
2017/18

The role of dynamic recrystallisation in the evolution of crystallographic preferred orientations of experimentally deformed calcite

Department of Earth Sciences, Utrecht University

Marina Galindos Alfarache
(Student number: 5893186)
30 ECTS

First Supervisor: **Dr. David Wallis**
Second supervisor: **Prof. Martyn R. Drury**

TABLE OF CONTENTS

ABSTRACT

The evolution of crystallographic preferred orientations (CPO) during dislocation mediated creep impacts many petrophysical properties and their anisotropy. Simulations and observations of CPO development in several minerals indicate that dynamic recrystallisation can exert a control on the types and strengths of CPO produced during deformation. However, experimental data constraining the impacts of each recrystallisation mechanism on calcite CPO are limited. For this reason, here I present electron backscattered diffraction (EBSD) measurements of CPO and other microstructures developed in experimentally deformed Carrara marble. The experiments were carried out at strain rates of 3×10^{-6} s^{-1} to 4.9×10^{-4} s^{-1}, temperatures of 700−990°C, confining pressures of 150 and 300 MPa, and to strains of 0.15−0.90 under uniaxial compression, triggering dynamic recrystallisation of the samples. Resultant flow stresses were in the range 15−85 MPa. The experiments resulted in different CPOs and microstructures, indicating variations in the deformation processes. At low temperature and high stress, grains are diamond shaped with mantles of subgrains indicating operation of grain boundary sliding (GBS) accompanied by subgrain rotation recrystallisation (SGR) and minor grain boundary migration (GBM). With increasing temperature and decreasing stress, grain boundaries become highly lobate, indicating a transition to recrystallisation dominated by grain boundary migration. This transition in grain morphology is accompanied by a transition in CPO, from a point maximum parallel to the compression axis to small circles or scattered point maxima. Misorientation axes of subgrain boundaries are parallel to {f}, {m}, (c) and/or <a>, all of which are consistent with tilt or twist boundaries comprised of dislocations on the {f}<0-111> and/or (c)<a> slip systems, indicating that one or both of these slip systems operated in all samples. These observations are broadly consistent with a model recently proposed based on observations of ice, in which (c)<a>, the weaker of the two slip systems above, is also the weakest slip system. At lower temperatures and/or higher stresses, subgrain rotation contributes to a [c]-axis maximum parallel to the compression axis. In contrast, at higher temperatures and/or lower stresses, GBM consumes grains that are poorly oriented for (c)<a>slip and therefore support higher stresses and dislocation densities than their neighbours. These results elucidate the control exerted by recrystallisation mechanisms on CPO type, which in turn impacts anisotropy in viscosity and seismic wave velocity.

1. INTRODUCTION

1.1 General background

Ductile deformation of crystals occurring at $T<1/2T_m$ is produced mainly by intracrystalline slip (Frost and Ashby, 1982). Slip systems are defined by a plane *hkl* and a direction *uvw*. The former is the plane with highest atomic density, whereas the latter is the close-packed direction within the slip plane. In a polycrystal, neighbouring grains impose to each other confining conditions that trigger the rotation of the crystal lattice with respect to an external coordinate system when slip happens on glide planes (Wenk *et al*., 1987). Consequently, changes in the orientation distribution of crystal directions occur. If the lattice orientation of crystal aggregates is distributed non-randomly, it describes a crystal preferred orientation (CPO).

The importance of the study of CPO resides on its impact in diverse physical properties. For instance, in the magnitude and anisotropy of viscosity (Castelnau *et al*., 2009; Hansen *et al*., 2016a; Hansen *et al*., 2016b), elastic (*i.e.*, seismic) properties (Zhang and Karato, 1995; Burlini *et al*., 1998; Cossette *et al*., 2015; Skemer *et al*., 2012; Hansen *et al*., 2014; Skemer and Hansen, 2015; Boneh *et al*., 2017), and thermal and electrical conductivity (Kocks *et al*., 2000). In addition, the study of rock microstructures and CPO has been widely used to infer the conditions (*e.g.,* temperature) accounted during rock deformation (Barnhoorn, 2003) and to discriminate the type and/or sense of deformation. Therefore, one can determine if the imposed strain was coaxial or non-coaxial (Barth *et al.*, 2010) and/or infer the sense of shear (Behrmann and Platt, 1982). Current hot topic is if or how can CPO elucidate the control exerted by determinate recrystallisation mechanisms. Therefore, the study of CPO is relevant not only to understand how CPO impacts on the anisotropical properties of rocks but also to infer active recrystallization mechanisms.

In order to understand the processes that are dominant during deformation events, a commonly approach has been to perform rock deformation experiments (*e.g.,* Griggs, 1936; Drury *et al.*, 1989; Walker *et al.*, 1990; Rutter *et al.*, 1994; De Bresser and Spiers, 1997; Ter Heege, 2002; Skemer and Hansen, 2015; Boneh *et al.*, 20017; Qi *et al.*, 2017). Those experimentalstudies aim to describe models which can be extrapolated into nature.

Ceramics and metallic minerals have been object of microstructural analysis, both for industrial (*e.g.,* metallurgy) interest and/or geological research. Some of the most studied minerals include quartz, olivine, calcite, salt, and more recently ice. The relevance of these minerals resides either in their abundance (*e.g.,* quartz in the crust and olivine in the mantle) or their implication on geodynamic processes (*e.g.,* calcite and salt in shear zones, and ice in glaciers).

Classical work on calcite deformation goes back to the XIX century where, for instance, Mügge (1883) discovered mechanical twinning on calcite. Years after, Orowan (1934), Polanyi (1934) and Taylor (1934) proposed independently that dislocations presented a major role on deformation and recrystallisation processes (Wenk and Christie, 1991). Moreover, modern studies are based on the polycrystal plasticity theory for minerals, which required at least five independent slip systems (Taylor, 1934) or one slip system (Sachs, 1928) within a grain in order to the rock to deform without internal cracking (Speight 1976). However, a deformed polycrystal needs to fulfil both stress equilibrium and strain compatibility so it can remain coherent. Analytical solutions are difficult to find, leading to either one or other assumption (known as lower bound limit and upper bound limit for stress respectively) (Wenk and Christie, 1991). On the other hand, comparison between natural and experimental textures have been performed for the lasts decades (*e.g.*, Wenk *et al*., 1987 for calcite) and major developments on EBSD and X-ray diffraction techniques has allowed further improvement on the knowledge of plastic

deformation in calcite (*e.g.*,Walker *et al*., 1990; Rutter *et al*., 1994; Barnhoorn, 2003) and other materials (*e.g*., Hansen *et al*., 2011 for olivine; Peternell *et al*., 2010 for quartz; or Qi *et al*., 2017 and Weikusat *et al*., 2017 for ice).

1.2 Problem definition

The aim of this project is to determine the role of dynamic recrystallization on the formation and/or evolution of CPO patterns in experimentally deformed marble at high temperature and strain conditions.

2. METHODS AND TECHNIQUES

2.1 Sample material

Calcite is a polymorph of calcium carbonate ($CaCO_3$) and an important rock forming mineral. Although sedimentary rocks are the most common calcite-rich rocks, they can also appear as volcanic (carbonatites) or metamorphic (marbles) rocks.

As a mineral, calcite belongs to the trigonal system, defined as 32/m or -3m (McKie and McKie, 1986) point group and R-3c space group. The crystal structure (Fig. 1A) is formed by a face-centered rhombohedron (Deer *et al.*, 1962; Phillips, 1962) containing four molecules. The rhombohedral cell is formed by the primitive rhombohedral (*i.e.,* structural cell) and the face-centered rhombohedral cell (*i.e.,* morphological cell), and it can be either be indexed with reference to the rhombohedral axes or the hexagonal axes (De Bresser,1991). In the present study I have chosen to work with the hexagonal structural cell (Fig. 1B), following the example of previous studies (*e.g.,* DeBresser, 1991; De Bresser and Spiers, 1990). Therefore, the hexagonal Miller-Bravais indices *hkil* and *uvtw* will be used in the oncoming chapters. The most common planes for calcite are summarized in Table 1. For the hexagonal system, lattice parameters are

$a = b = 4.99$ Å, $c = 17.06$ Å, $\alpha = \beta = 90°$ and $\gamma = 120°$ (Cornelius and Cornelis, 1997).

The early works of Turner *et al.* (1954) and Griggs (1960) evidenced that there is a dominant twinning system and two slip systems for calcite:

(i)   twinning on $e\{-1018\}<40\text{-}41>^+$. Composed by three systems.

(ii)   slip on $r\{10\text{-}14\}<\text{-}2021>^\pm$. Composed by three systems.

(iii)   slip on $f\{-1012\}<2\text{-}201>^\pm$. Composed by six systems.

where the {*hkil*}<*uvtw*> notation indicates the family of the twinning/slip system. The plane is indicated by the symbol {} whereas <> indicates the direction. For individual slip system (*hkil*) and [*uvtw*] symbols are used instead. The ± superscript points out the slip sense.

The subsequent works of Turner and Heard (1965a) and Paterson and Turner (1970) revealed that slip on $a\{-12\text{-}10\}<\text{-}2021>$ was also possible and Thomas and Renshaw (1967) found the same results for slip on $m\{10\text{-}10\}<\text{-}12\text{-}10>$. More recent studies (De Bresser and Spiers, 1997) indicated that
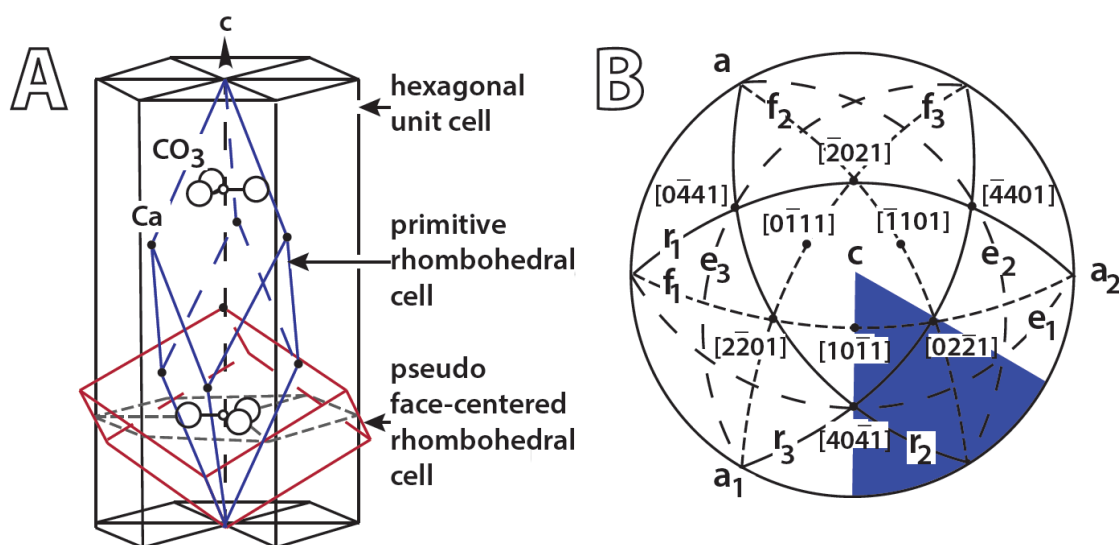

Figure 1. a) Different type of cells within a calcite crystal; and **b)** crystallographic projection of the different planes within calcite (De Bresser, 1991). Unit cell has been marked in blue.

Table 1. Cell parameters and planes conforming the structure of calcite (De Bresser, 1991)

Planes	Hexagonal structural cell	Hexagonal morphological cell	Rhombohedral structural cell	Rhombohedral morphological cell
c	0001	0001	111	111
e1	-1018	-1012	233	011
e2	1-108	1-102	323	110
e3	01-18	01-12	332	110
f1	-1012	-2021	011	-111
f2	1-102	2-201	101	1-11
f3	01-12	02-21	110	11-1
r1	10-12	10-11	211	100
r2	-1104	-1101	121	010
r3	0-114	0-111	112	001
m1	10-10	10-10	2-1-1	2-1-1
m2	-1100	-1100	-12-1	-12-1
m3	0-110	0-110	-1-12	-1-12
a1	2-1-10	2-1-10	1-10	1-10
a2	-12-10	-12-10	01-1	01-1
a3	-1120	-1-120	-101	-101

Intersections				
r1:r2	0-441	0-111	-1-13	001
r2:r3	40-41	10-11	3-1-1	100
r1:r3	-4401	-1101	-13-1	010
f1:f2	02-21	01-12	11-1	110
f2:f3	-2021	-1012	-111	011
f1:f3	2-201	1-102	1-11	101
a1:f3	0-111	0-114	001	112
a2:f1	10-11	10-14	100	211
a3:f2	-1101	-1104	010	121

Cell parameters			
Hexagonal structural cell:	a =4.99Å	c =17.06 Å	
Hexagonal morphological cell:	a =19.96Å	c =17.06 Å	
Rhombohedral structural cell:	aRH=6.37Å	α=46.05°	
Rhombohedral morphological cell:	aRH=12.85Å	α=101.55°	

for temperatures >400°C there are two additional subsidiary glide systems: $f\{-1012\}<10-11>$ and basal $c\{0001\}<-12-11>$; being (c)<a> the easiest slip system of the two. Table 2 summarizes the quoted twinning and slip systems.

Calcite deforms crystal-plastically at relatively low P-T conditions, which makes it a suitable test sample for deformation experiments (Bestmann *et al.*, 2000; Pieri *et al.*, 2001). Furthermore, calcite typically deforms under the dislocation creep regime (Wenk *et al.*, 1987; Renner *et al.*, 2002). Moreover, Ter Heege (2002) reported that the samples of this study were affected by dislocation-controlled cross-slip of dislocations (Fig. 2).

Marble is a polycrystalline aggregate. Although calcite is not the most abundant rock-forming mineral–it only represents the 4% wt. of the

crust−carbonate rocks are often involved in lithosphere scale shear zones and seismic events in the upper crust (Barnhoorn *et al.*, 2005; Smith *et al.*, 2011). The mechanical weakness of calcite causes the early deformation of carbonate rocks relative to other lithologies during geodynamic events such as mountain building or subductions. Consequently, the deformation microstructures formed on calcite are very often the only observable indicators of the conditions and mechanisms accounted during deformation.

For the study of calcite, Carrara marble is one of the standard rocks used in rock deformation experiments. The suitability of this material resides in the homogeneity of its initial microstructure, with absence of CPO. Hence, the microstructures observed after finalizing the deformation experiment are representative of the experimental

conditions (Ter Heege, 2002). Carrara marble is a pure coarse grained material which deforms dominantly by intracrystalline plastic flow in addition with dynamic recrystallisation at T>600°C (Rutter 1974; Schmid *et al.*, 1980; Covey-Crump, 1998, Ter Heege, 2002). Consequently, Carrara marble develops subgrains and recrystallised grains at high temperatures (Schmid *et al.*, 1980; Rutter, 1995; De Bresser, 2002) and has clear backscattered diffraction patterns (Valcke, 2008). Therefore, Carrara marble not only allows specific and well-designed experiments due to the large compiled knowledge of its rheology, but it is an ideal material to study with electron backscattered diffraction (EBSD) techniques.

The samples investigated in this study are a Lorano Bianco type of marble, original from a Cararra marble block from Alpi Apuane in Italy (Ter Heege, 2002; Valcke, 2008). In the works of Molli *et al.* (2000) and Pieri *et al.* (2001) the structural elements, chemical composition and material properties are described, as well as the structure, stratigraphy and tectonics of the rock source area. The marble contains ~99% calcite and minor traces of muscovite, quartz, dolomite and graphite (Ter Heege, 2002; Valcke, 2008). The samples were subjected to static annealing prior to the experiments, in order to eliminate any possible pre-microstructures. However, a weak shape preferred orientation was reported after the annealing (Ter Heege, 2002).

Table 2. Calcite's most common twinning and slip systems (De Bresser and Spiers, 1997)

Twinning systems
e^+ {-1018}<40-41>
r^+ {10-14}<-2021>
f^- {-1012}<-101-1>

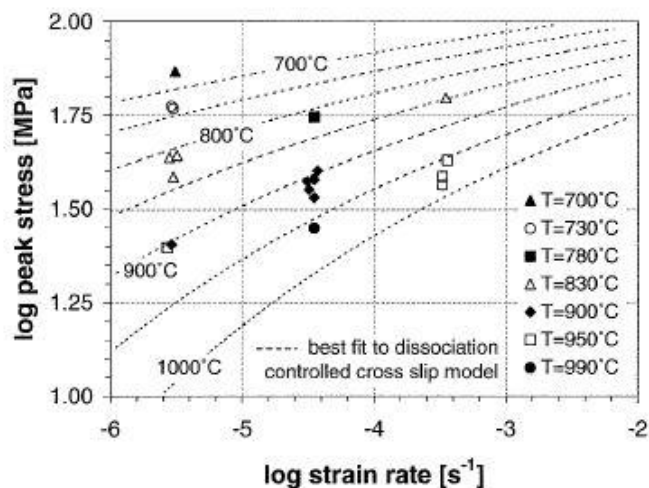| Slip systems: |
| --- |
| r {10-14}<-2021> |
| f {-1012}<2-201> |
| f {-1012}<10-11> |
| a {-12-10}<-2021> |
| c [0001]<-12-10> |
| m {10-10}<-12-10> |

Figure 2. Plot relating peak stress and strain rate. The curved morphology of the dashed best fit lines indicates that dislocations are cross-slip controlled (Ter Heege, 2002).

2.2 Experimental deformation of the samples

Ter Heege (2002) and Valcke (2008) performed deformation experiments over 23 samples (Table 3). They were deformed in a constant volume, internally heated argon gas medium apparatus by constant displacement rate tests. The experiments were carried out at strain rates of 3×10^{-6} s^{-1} to 4.9×10^{-4} s^{-1}, temperatures of 700−990°C, confining pressures of 150 and 300 MPa, and to strains of 0.15−0.45 under uniaxial compression, triggering dynamic recrystallisation of the samples. Resultant flow stresses were in the range 15−85 MPa. Samples were immediately cooled at 70°C/min after experiments to limit post-deformation annealing (Ter Heege, 2002). The deformed samples were cut and sliced parallel to the maximum compression direction for all samples.

One sample (36/LM900/0.9, here addressed as sample 37) was deformed to a natural strain of 0.90 in three subsequent tests on the same sample. This implied the removal of the sample twice from the gas apparatus and jacket; after re-polishing and re-jacketing the sample was inserted again in the apparatus and heated to 900°C before restoring the load.

2.3 Data acquisition

The use of light microscope is very common on the analysis of textures (*i.e.,* CPO). However, there was available for the purpose of this study a large EBSD dataset compiled by a previous study of these samples (Valcke, 2008). In consequence, I have decided to place aside the use of light microscope and focus on the challenge of taking maximum advantage of computational tools. Therefore, I am going to analyse exclusively EBSD data. EBSD is a scanning electron microscope (SEM) based technique that gives crystallographic information about the microstructure of a sample.

The information is obtained after the interaction of a stationary electron beam with a tilted sample (70° from the horizontal). The diffracted electrons form a pattern detected by a fluorescent screen. This pattern is characteristic of the crystal structure and orientation of the analysed sample region. From these patterns some information can be extracted, for instance crystal orientation, discrimination of different phases, characterization of grain boundaries, or information of local crystalline imperfections. Consequently, the resulting maps reveal the grain morphology, orientations and boundaries. In addition, information about CPO can also be obtained. Therefore a complete quantitative representation of the microstructure can be established with EBSD.

The orientations of the samples relative to the crystal are described by a set of Euler angles.

Table 3. Summary of previous data for my samples collected by Ter Heege (2002) and Valcke (2008). N_D refers to number of deformed grains; N_X refers to number of recrystallised grains; and GS refers to grain size. In this study I will name the samples by the number presented in the second column

Sample ID [Ter Heege/ Valcke]	Sample ID [Galindos]	peak stress [MPa]	Final Stress [MPa]	Natural strain	T [°C]	Exp. Strain rate [s⁻¹]	ND	deformed GS [µm]	NX	recrystallised GS [µm]	bulge size [µm]	exp. Duration [h]
15LM950/0,45	31	24,9	14,6	0,45	962	4.2×10^{-6}	57	84,7	80	37,2	-	39,07
25LM900/0,45	44	25,4	21,8	0,42	906	3.9×10^{-6}	545	35,5	325	13,8	13,2	38,12
25LM950/0,45	SV05	24,8	24,8	0,45	950	-	60	61,3	44	10,0	10,4	-
25LM990/0,45	41	25,0	28,1	0,45	992	4.6×10^{-5}	93	45,7	79	14,8	11,3	-
36LM830/0,15	28	38,5	36,7	0,17	829	-	77	69,4	50	11,5	10,4	17,41
36LM830/0,30	29	43,9	39,6	0,29	830	3.4×10^{-6}	218	35,8	211	7,4	8,9	27,95
36LM830/0,45	40	43,4	38,7	0,45	835	4×10^{-6}	508	26,4	546	9,0	10,9	40,09
36LM900/0,15	21	37,4	34,1	0,16	903	3.7×10^{-5}	83	68,3	61	8,3	9,7	1,7
36LM900/0,30	24_2a	35,6	32,9	0,27	901	4×10^{-5}	65	58,4	38	7,0	10,1	2,14
36LM900/0,45	27	39,9	36,3	0,40	898	4.5×10^{-5}	164	29,6	146	10,7	9,9	2,98
36LM900/0,90	37	33,9	26,2	0,90	902	7.1×10^{-5}	854	21,7	672	9,6	10,1	-
36LM950/0,15	22	36,7	35,2	0,16	960	4.2×10^{-6}	76	65,0	49	9,4	9,9	0,08
36LM950/0,30	26	38,5	32,5	0,30	957	-	62	56,2	71	13,7	9,7	0,23
36LM950/0,45	25	42,6	31,6	0,46	949	-	202	42,6	151	9,9	8,7	0,33
50LM730/0,45	43	58,5	52,1	0,44	731	3.9×10^{-6}	607	22,0	604	7,7	8,9	39,56
50LM780/0,45a	34_1	55,6	47,3	0,43	776	4.7×10^{-5}	333	34,4	277	11,6	8,0	3,21
50LM780/0,45b	34_2	55,6	47,3	0,43	776	4.7×10^{-5}	387	36,2	328	11,0	8,1	3,21
50LM830/0,45	33	62,6	53,3	0,44	830	4.7×10^{-4}	318	33,3	207	11,3	7,6	0,33
50LM900/0,45	SV02	56,2	44,4	0,40	900	-	173	39,9	134	29,8	-	-
65LM700/0,45	35	73,5	65,0	0,43	689	3.8×10^{-6}	720	21,6	678	7,5	7,9	39,44
85LM730/0,15	SV04	88,8	89,3	0,15	735	-	71	77,9	75	5,2	7,6	-
85LM730/0,30	SV03	91,4	88,5	0,28	735	-	175	43,1	169	5,1	7,2	-
85LM730/0,45	SV01	88,7	82,1	0,42	735	-	308	22,8	419	5,8	6,9	-

Orientation maps−or Euler maps−are obtained by plotting the 3 Euler angles by using a RGB colour scheme. EBSD analysis can also measure the misorientation (*i.e.,* difference in orientation) between two crystals. The misorientation axis-angle pair is equivalent to the rotation axis-angle pair which maps one crystal lattice onto the other. However, for crystals with some symmetry there is no longer a unique axis-angle pair that describes the misorientation between 2 crystal lattices, but up to 24 symmetrically equivalent axis-angle pairs. Therefore, since it is not possible to determine which of the different solutions is correct, the convention is to take the solution of the lowest misorientation angle (*i.e.,* disorientation angle) (Wheeler *et al*., 2001)

For this study, EBSD data were collected by using a Philips XL30SFEG SEM with a Nordlys 2 CCD camera. SEM conditions were a beam of 20 kV, a beam current of 2 nA, and a working distance of 15 mm for a 70º tilted sample. This resulted in general high indexing success rates (>90%) (Valcke, 2008). The obtained maps have a size of 1000x1000 μm. The number of points for each picture is 10^6 and a step size of 1 μm. Valcke (2008) reported that although resolution was enough to map the smallest subgrains, angular resolution limited the subgrain misorientation angles. The term "noise" is defined as random misorientations that are not related to the structure. Valcke (2008) noted that subgrain boundaries <1° were difficult to discriminate from noise. However, low angle noise ~1° could be reduced sufficiently by using the method of Cao *et al.* (2003).

2.4 Data analysis

2.4.1 Software

The analysis of the data has been done with both HKL Channel 5 and MTEX software. The former has been developed by Oxford Instruments HKL Technology and it includes a set of packages designed to manipulate, analyse and display EBSD data. The packages used in this study are called Tango and Mambo and their function is to display maps and work with (inverse) pole figures respectively. Channel 5 is designed in a way that the multiple packages are interconnected. Therefore, when one modification is applied in one of the packages there is an automatic redisplay of the data on the rest of packages. Channel's 5 package Tango is an ideal tool to perform and combine maps. Several options can be displayed, based on i) grid components, ii) boundary components, and iii) grain components. For instance, in grid components the software allows to display local misorientation, Euler or Schmid factor maps whereas in boundary components it allows to define (sub) grain by different colours and/or thickness. In this study I have used the options for: i) band contrast, indicating larger deformed regions with low band contrast values; grain boundary, defining (sub) grain boundaries; and inverse pole figures (IPF), to determinate the sample coordinate distribution on the Y direction with respect to the crystal reference frame. In addition, grain size measurements can be done with a wide range of results including grain size distribution or individual values for area, diameter or aspect ratio among others. Tango also allows grain shape characterization based on i) grain area, ii) the circle equivalent diameter, or iii) the major and minor axis of fitted ellipse. However, these analysis are relatively simple compared to other such as PARIS factor (Heilbronner and Barret, 2014), which can provide more accurate shape descriptions. Finally, Tango also permits to define each grain as a single point with the "one point per grain" option. This constitutes an advantage when plotting pole figures on Mambo since the amount of projected values is representative of the number of grains in the sample. If not, larger grains would have a bigger impact over small grains in pole figure projections.

On the other hand, MTEX is a toolbox which can be executed on MATLAB® and was created by Ralf Hielscher in 2002. Further development has been done with the additional collaboration of F. Bachmann, O.K. Johnson and D. Mainprice. MTEX

is a free software which can be downloaded online and has periodical updates. The website also provides with multiple examples. MTEX is used to analyse and create models of crystallographic textures by using EBSD or pole figure data.

MTEX provides a wider range of analysis compared to Channel 5, including: i) microstructure analysis (PolyLX), including crystal geometry, tensors, and ODFs among other EBSD analysis; ii) fabric analysis (FAME); iii) slip transfer analysis (Stabix); and iv) seismic anisotropy analysis (MSAT). The programming nature of MTEX constitutes and advantage since it allows parallel multidisciplinary analysis.

2.4.2 Grain analysis

I have done several distinctions regarding grain analysis. These have been done with the band contrast and (sub) grain boundary map on Tango. Firstly, I have optically distinguished a bimodal grain size distribution for all the samples. I will use the term "porphyroclast" or "larger grains" to refer to those grains deformed under the experimental strain conditions and the term "recrystallised" to refer to those grains formed during dynamic recrystallisation. Secondly, I have defined the recrystallised fraction as grains with misorientation angle θ>15° and subgrains with θ<15° (Fig. 3). Typically, the limit misorientation angle is defined as 10° for geological studies and 15° for studies in metals. However, I have checked that slightly differences are obtained by using 10 or 15°, so I have decided to use 15° to incorporate a wider spectrum.

Furthermore, although Table 3 provides with more detailed measurements of deformed and/or recrystallised grain size I have decided to make an average calculation based on the linear intercept method (Table 4). Therefore, I have used 250 lines in both vertical and horizontal directions and stablished 15° as the misorientation limit between grain boundaries.
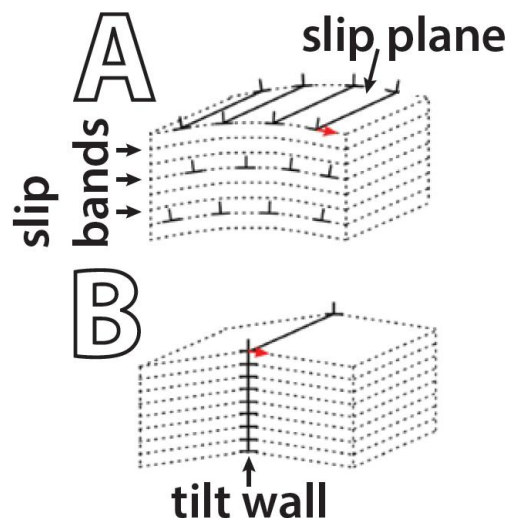
Figure 3. Formation of a stacking fault by glide and accumulation of edge dislocations. The stacking fault or tilt boundary separates two differentiated grains (*i.e*., the original grain from a recrystallised grain) when θ>15° whereas separates the original grain from a subgrain at θ<15°. Red arrow indicates the Burgers vector of the tilt wall (Wallis *et al*., 2017).

Finally, I have analysed the shape of the grains by using the percentile average relative indented surface (*i.e.*, PARIS factor). PARIS consists on a method to quantify the amount of indentations of a grain by measuring the grade of convexity-concavity of the grain boundary (Panozzo and Hürlimann, 1983; Heilbronner and Barret, 2014). Therefore−ideally− fully convex shapes will have a value of 0% whereas increasing values will be obtained with increasing irregularity of the grain boundary. Mathematically is expressed as:

$$PARIS = \frac{1}{n}\sum_{i=1}^{n}\frac{A(\alpha_i)-2B(\alpha_i)}{B(\alpha_i)} \qquad (1)$$

where A is the cumulative length of the outline of a polygon , projected segment by segment, and B is the total length of projection (*i.e.,* difference between x-coordinate maximum and minimum) (Fig. 4). If the shape presents a convex-concave outline A(α) exceeds 2B(α) (Heilbronner and Barret, 2014).

Table 4. Average PARIS values calculated for each sample and classification in its respective grain shape group, note that optical criteria has been decisive for final validation. Additional information on number of grain and average grain size has been included based on the linear interception method with 250 lines for a critical misorientation of 15° both horizontally (EX horizontal) and vertically (EX vertical)

Sample	Average (PARIS)	Classification	number of grains	EX Horizontal	EX Vertical	Average
Starting material	-	-	456	72,692	81,788	77,240
31	38,720	L2	457	64,620	61,026	62,823
44	41,851	L1	875	28,487	35,560	32,024
SV05	21,377	L2	289	79,220	66,870	73,045
41	34,717	L2	610	72,187	58,202	65,195
28	33,432	L2	268	67,895	74,465	71,180
29	38,546	D	695	50,212	54,825	52,519
40	39,732	D	1418	35,365	33,084	34,225
21	35,411	L2	318	59,278	76,206	67,742
24_2a	32,155	L2	268	71,317	91,089	81,203
27	32,986	L2	365	68,549	53,603	61,076
37	36,662	D	1542	27,164	33,637	30,401
22	32,208	L2	671	58,872	64,772	61,822
26	31,547	L2	297	66,774	82,057	74,416
25	42,217	L1	562	52,386	38,722	45,554
43	38,070	D	1009	37,525	35,991	36,758
34_1	42,700	L1	721	38,310	30,824	34,567
34_2	45,066	L1	814	32,834	28,161	30,498
33	46,728	L1	581	40,356	33,677	37,017
SV02	34,147	L2	410	50,318	39,082	44,700
35	44,386	D	1388	28,438	35,827	32,133
SV04	32,245	D	314	65,366	73,016	69,191
SV03	35,776	D	360	58,723	74,982	66,853
SV01	38,459	D	596	70,571	52,240	61,406

I have used this concept to separate lobate grains from angular/diamond-shaped grains. Although PARIS factor has been calculated for all the samples, I must point out that additional optical discrimination was required for final classification validation.

2.4.3 Pole figures

Pole figures (PF) provides information on the distribution of single crystal directions with respect to a sample reference frame (Wenk *et al.*, 1987). Consequently, to determine the distribution of crystal directions relative to the compression direction I have done stereographic projections of
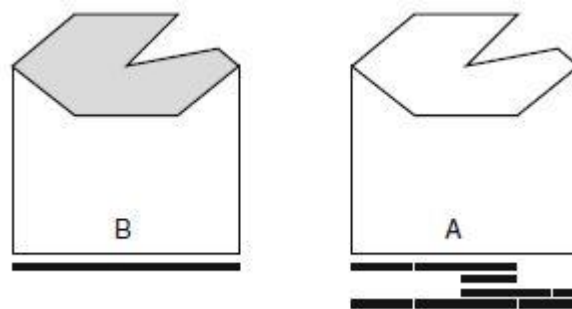
Figure 4. Outline projection of convex-concave shapes, where A represents the surface projection (*i.e.*, segment by segment) and B the particle projection shape (Heilbronner and Barret, 2014).

the [*c*]-axes for the *c*(0001) and *f*{-1012}<10-11> slip planes, which are expected to be the most active at the present experimental conditions (De Bresser and Spiers, 1997). Twin *e*{-1018}<40-41> has been excluded from the analysis since its activity at this temperature conditions is not meaningful (De Bresser, 1991).

Data was analysed by considering one point per grain, a half width of 10º and a cluster size of 5º. Pole projections were done in lower hemisphere, equal area projection and coordinate system was established as X direction on the east, Y direction on the north, and Z direction out of plane. Pole density was measured by means of multiples of uniform density (m.u.d.). Note that m.u.d. is a relative measure, calculated with respect to the amount of neighbouring poles. Consequently, the scale value varies from one sample to another and so scale bars are included for each sample.

CPO strength has been measured quantitatively by using several methods. Firstly I have measured the J-index (Bunge, 1982), which scale varies from 1 to infinity, where CPO strengthens towards infinity. It is defined as the second moment of an orientation distribution function (ODF) (Skemer *et al.*, 2005), where ODF is the distribution of discrete crystal orientation data in Euler angle space. However, Skemer *et al.*(2005) argued that the interpretation of this parameter can often be difficult to interpret due to its highly sensitivity to the amount of grains as well as the arbitrary smoothing factors that are applied in this calculation. In addition, Wenk (2002) also argued that meaningful results would only be obtained by analysing an impractically large number of data. For these reasons, Skemer *et al.* (2005) proposed the misorientation-index (M-index) as an alternative measure of CPO strength. Misorientation angles are expected to shift towards small angles ($\theta<15°$) at increasing deformation and CPO development due to progressive alignment of grains (*i.e.*, many grains having similar orientations) (Wheeler *et al.*, 2001). Based on this premise, the M-index provides an indicator of the distribution of misorientation orientations,

insensitive to the numerical parameters used in its calculations (Skemer *et al.* 2005). M-index is up to 1, so values ~0 indicate random distributions and ~1 strong CPO.

Additional measurements have been done based on eigen-values and eigen-vectors calculations. Woodcock (1977) proposed a fabric plot with two axes corresponding to cluster (ln($\lambda1/ \lambda2$)) and girdle (ln($\lambda2/ \lambda3$)) distributions. From this plot two parameters can be extracted: the C-index, which is a measure of fabric strength; and the K-index, which measures the CPO shape.

$$C = \ln\left(\frac{\lambda1}{\lambda3}\right) \qquad (2)$$

$$K = \ln\left(\left(\frac{\lambda1}{N}\right)\Big/\left(\frac{\lambda2}{N}\right)\right)\Big/\ln\left(\left(\frac{\lambda2}{N}\right)\Big/\left(\frac{\lambda3}{N}\right)\right) \qquad (3)$$

Both index ranges from 0 to positive infinity and $\lambda1$, $\lambda2$ and $\lambda3$ are the eigenvalues calculated from a matrix where $\lambda1 \geq \lambda2 \geq \lambda3$, and $\lambda1 + \lambda2 + \lambda3 =N$. $\lambda1$ is the mean or best-fit axis of the data (Scheidegger, 1965) and the strength and symmetry of the fabric is determinate by the relative magnitude between the eigenvalues (Watson, 1966).

Point (P) $\lambda1 > \lambda2 \sim \lambda3$ (4)

Girdle (G) $\lambda1 \sim \lambda2 > \lambda3$ (5)

Random (R) $\lambda1 \sim \lambda2 \sim \lambda3$ (6)

On the other hand, Vollmer (1990) proposed a similar analysis to the plot proposed by Woodcock (1977) in form of a triangle diagram. Vollmer (1990) argued that his triangle was a better solution since it is a closed representation with three end-members describing the different orientation distributions (Fig. 5). The difference between both methods resides on the comparison between eigenvalues for the Vollmer method against the comparison between ratios for the Woodcock method. Thus, the end-members of the triangle are point (P), girdle (G), and random (R) and the matrix
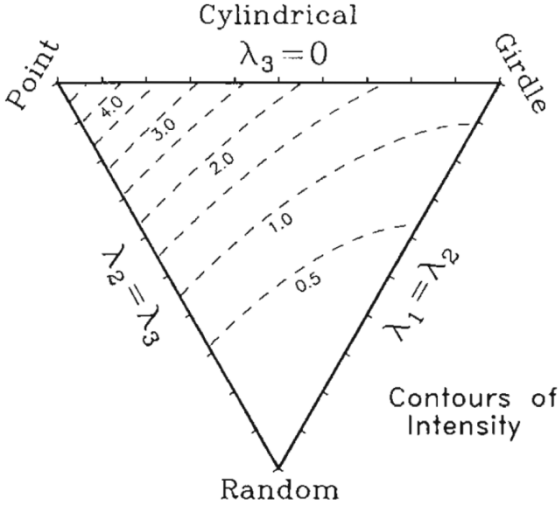
Figure 5. Triangular projection with three end members to represent the fabric distribution of orientation data based on the measure of eigenvalues. (Vollmer, 1990).

is described as:

Point   [N 0 0]   (7)

Girdle   [N/2 N/2 0]   (8)

Random   [N/3 N/3 N/3]   (9)

However, if the three components are given equal weight then the indexes can be described as:

$$P = \frac{(\lambda 1 - \lambda 2)}{N} \tag{10}$$

$$G = 2 \cdot \frac{(\lambda 2 - \lambda 3)}{N} \tag{11}$$

$$R = 3 \cdot \frac{\lambda 3}{N} \tag{12}$$

where P+G+R=1. These indexes range from 0 to 1, where 0 stands for random and 1 for either perfect girdle or point distribution (Vollmer, 1990).

2.4.4 Inverse pole figures

Inverse pole figures (IPF) indicates which crystallographic direction aligns with a specific sample axes. In other words, it shows the pole that

is parallel to a given reference direction.

On one hand, I have done IPF projections on EBSD maps (*i.e.*, on the Y direction) and stereographic projections for all samples. IPF stereographic projections have been plotted in upper hemisphere equal area projection. Due to symmetry, only the unit triangle has been plotted. The contouring was done with a half width of 10º and a cluster size of 0º. Contouring densities are expressed in m.u.d.

On the other hand, I have also plotted the IPF for misorientations between 1 and 15º (*i.e.,* subgrains).

Intragranular misorientations are produced by the presence of dislocations and its analysis can provide an insight of the active slip systems. The analysis consists on defining the crystallographic directions at which the misorientation axis aligns with. The misorientation axes have been plotted in crystal reference frame (MIPF) and upper hemisphere equal area projection. The contouring was done with a half width of 10º and a cluster size of 0º. Contouring densities are expressed in m.u.d.

2.4.5 Schmid factor

Considering that slip occurs by dislocation motion, this will only occur when a certain amount of shear stress is applied. The resolved shear stress (RSS) is the shear component of an applied stress (Fig. 6).

$$\tau = \sigma \cdot \cos \theta \cdot \cos \emptyset = \sigma \cdot m \tag{13}$$

where τ is the RSS, θ is the angle between slip direction and applied force, ϕ is the angle between normal of slip plane and applied force, and m is the Schmid factor (SF). SF is a quantitative method to describe the relationship between the RSS and the applied stress (Wallis *et al*., 2018). Or in simpler words, the component that describes the distribution of shear stress in the different slip systems.

I have analysed the activity of the several slip systems based on the determination of SF. Slip in a

determinate plane is more favourable when SF values are high (*i.e.,* higher RSS). θ and ϕ are complementary, and the largest angle for each of them is 45°, resulting in a maximum of 0.5 for SF.

I have mapped the (*c*), {*r*}, {*f*}<2-201>, and {*f*}<10-11> slip systems for each sample with respect to the SF. This will allow me to visualize which grains are best oriented for dislocation glide and which is the preferred family of slip systems.
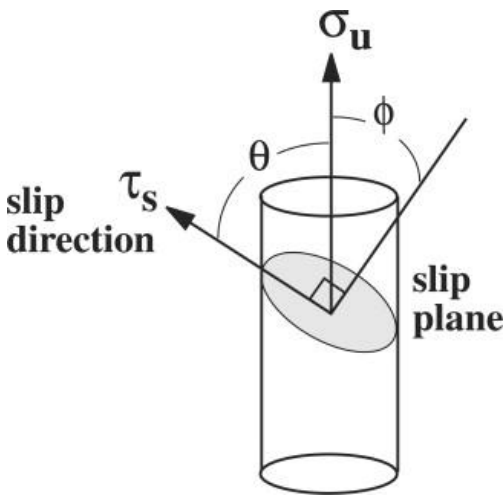
Furthermore, minimum SF represents the minimum stress necessary to enhance slip. This parameter depends on the critical resolved shear stress (CRSS). Both values have been calculated and are collected in Table 5. CRSS has been calculated based on the equations of De Bresser and Spiers (1997):

$$\tau_c^{(r)} = 10^{10.36 \pm 0.36} \, T_{abs}^{-3.27 \pm 0.13} \qquad (14)$$

$$\tau_c^{(f-LT)} = 10^{7.56 \pm 1.78} \, T_{abs}^{-2.12 \pm 0.11} \qquad (15)$$

$$\tau_c^{(f-HT)} = 10^{16.22 \pm 1.47} \, T_{abs}^{-5.05 \pm 0.50} \qquad (16)$$

$$\tau_c^{(c)} = 10^{7.54 \pm 6.17} \, T_{abs}^{-2.24 \pm 2.05} \qquad (17)$$

Figure 6. Representation of the concept behind RSS and Schmid factor. The shear component of an applied stress over a plane varies in function of the orientation of such plane.

where τ_c is the CRSS and is expressed in MPa, and

T_{abs} is expressed in Kelvins.

2.4.6 Separation of the recrystallised fraction

Since the sample presents a bimodal distribution I have separated the recrystallised fraction from the whole sample (referred now on as bulk fraction) to see if the (I)PF differs in each fraction.

The separation has been done in different steps. Firstly I have calculated the grain sizes for each grain of the sample. I have taken the inflexion threshold between small and big grain sizes as the limit between recrystallised grains and porphyroclasts. Afterwards, I have used the "local misorientation" option to plot misorientations ranged between 1and 15° and manually I have included those strain free grains in the recrystallised subfraction. The residual grains were included in the porphyroclast subfraction.

Five random samples have been analysed for this purpose. All of them show the same results. The CPO and IPF results for the recrystallised fraction resembles more to the bulk results. However the difference between the results from the recrystallised fraction and the porphyroclasts is very low. Therefore, I can consider that the bulk results are representative for both subfractions and thus I will analyse each fraction in their whole bulk. These results can be observed in an example for sample 25 in Figure 7.

Table 5. Values for critical resolved shear stress (CRSS) and minimum Schmid Factor for each of the samples. Notice sample 31 has a minimum SF>0.5 for *f*<2-201>

| sample | Δσ [Mpa] | T abs [K] | CRSS [MPa] | | | | Min Schmid Factor | | | |
			r	f <2-201>	f <10-11>	c	r	f <2-201>	f <10-11>	c
35	65	973	3,88	16,80	13,49	7,02	0,060	0,259	0,208	0,108
43	50	1003	3,51	15,75	11,57	6,56	0,070	0,315	0,231	0,131
SV01	85	1003	3,51	15,75	11,57	6,56	0,041	0,185	0,136	0,077
34_1	50	1053	3,00	14,21	9,05	5,89	0,060	0,284	0,181	0,118
34_2	50	1053	3,00	14,21	9,05	5,89	0,060	0,284	0,181	0,118
29	36	1103	2,58	12,87	7,16	5,30	0,072	0,358	0,199	0,147
40	36	1103	2,58	12,87	7,16	5,30	0,072	0,358	0,199	0,147
33	50	1103	2,58	12,87	7,16	5,30	0,052	0,257	0,143	0,106
44	25	1173	2,11	11,30	5,25	4,62	0,084	0,452	0,210	0,185
21	36	1173	2,11	11,30	5,25	4,62	0,059	0,314	0,146	0,128
24_2a	36	1173	2,11	11,30	5,25	4,62	0,059	0,314	0,146	0,128
27	36	1173	2,11	11,30	5,25	4,62	0,059	0,314	0,146	0,128
37	36	1173	2,11	11,30	5,25	4,62	0,059	0,314	0,146	0,128
SV02	50	1173	2,11	11,30	5,25	4,62	0,042	0,226	0,105	0,092
31	15	1223	1,84	10,34	4,25	4,21	0,123	0,689	0,283	0,281
SV05	25	1223	1,84	10,34	4,25	4,21	0,074	0,414	0,170	0,168
22	36	1223	1,84	10,34	4,25	4,21	0,051	0,287	0,118	0,117
25	36	1223	1,84	10,34	4,25	4,21	0,051	0,287	0,118	0,117
41	25	1263	1,65	9,66	3,61	3,92	0,066	0,386	0,144	0,157
26	36	1223	1,84	10,34	4,25	4,21	0,051	0,287	0,118	0,117
28	36	1103	2,58	12,87	7,16	5,30	0,072	0,358	0,199	0,147
sv03	85	1003	3,51	15,75	11,57	6,56	0,041	0,185	0,136	0,077
sv04	85	1003	3,51	15,75	11,57	6,56	0,041	0,185	0,136	0,077
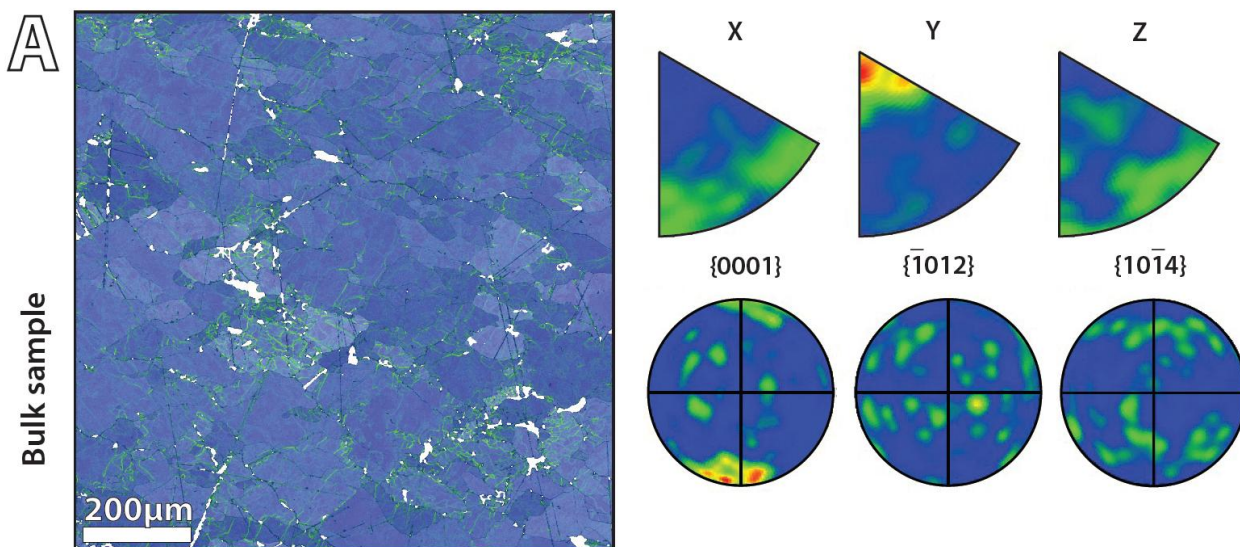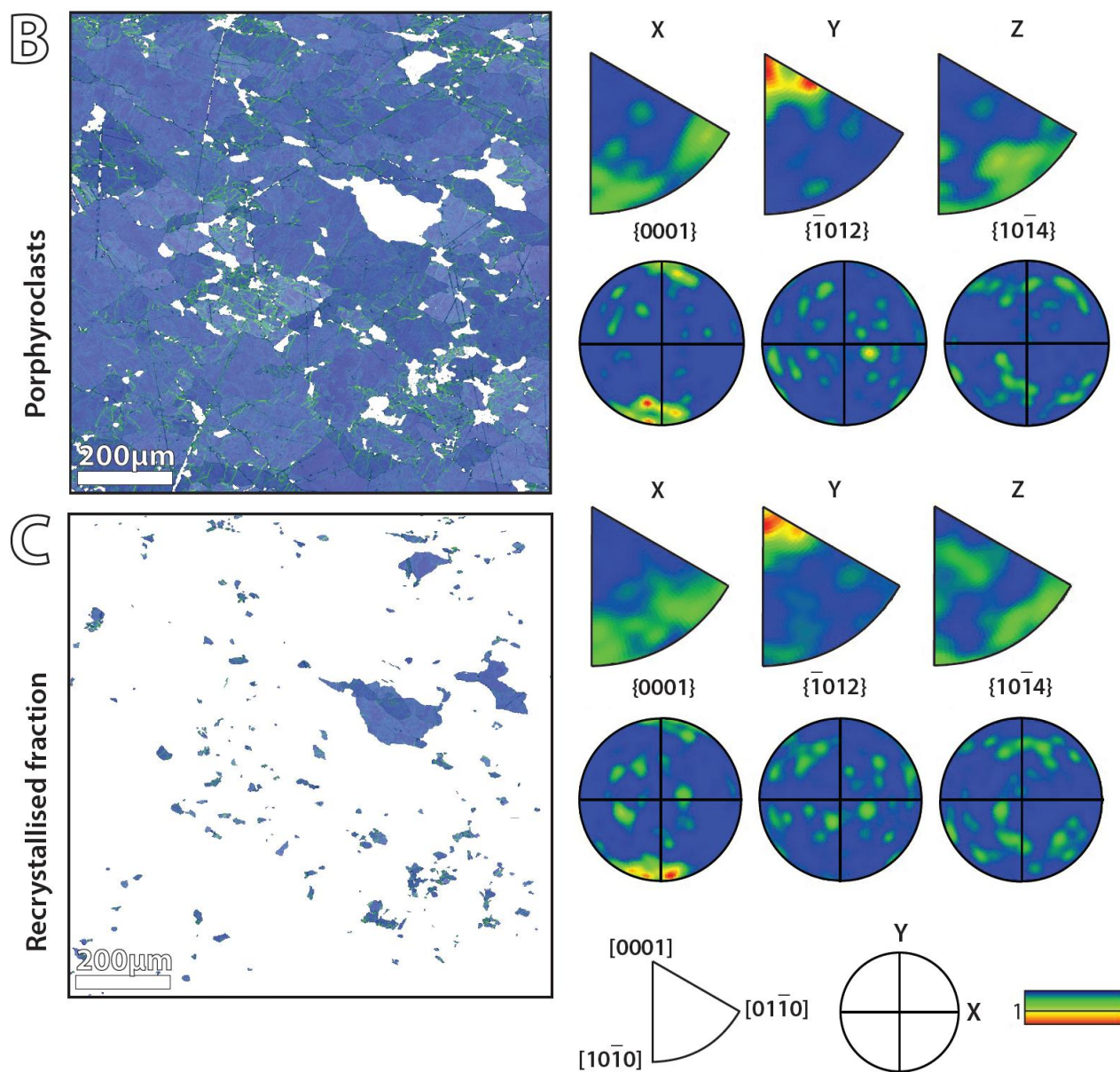
Figure 7. Comparaison between: **a)** bulk fraction; **b)** porphyroclast fraction; and **c)** recrystallised fraction. It can be observed in both IPF and PF that all three samples present almost identical results.

3. RESULTS

2.5 Microstructures

The samples reveal a transition from angular/ diamond-shaped grains to lobate grains (Fig. 8). In this study I will refer to the first ones as type D and the latter as type L1 or L2 depending on the microstructure. L1 microstructures are composed by big lobate porphyroclasts in addition to an elevated amount of small grains whereas L2 is apparently formed by even larger porphyroclasts and fewer small grains.

Therefore, by combining PARIS factor and optical criteria I have defined samples 29, 35, 37, 40, 43, SV01, SV03, and SV04 as type D; samples 25, 33, 34_1, 34_2, and 44 as type L1; and samples 21, 22, 24, 26, 27, 28, 31, 41, SV02, and SV05 as type L2 (Table 4). For PARIS values >40% grain shapes are predominantly of type L1, with exception of sample 35. On the other hand, for values >35.5% the microstructures are representative of type D grains, except for sample 31. Below 35.5%, grain shapes have been defined as L2, except for sample SV04.

Moreover, as a result of the linear interception measurement, it can be observed that the bulk grain size is reduced for all samples except for that of sample 24_{2A} (Table 4). However, we must take into account that this measurement does not separate different fractions. Therefore, if comparing just the grain size of porphyroblasts to the undeformed grains it can be noticed that type D and L1 are very similar to the starting material whereas L2 decreases in size. For instance, the average diameter of the starting material is ~200µm; for SV01 (type D) and sample 33 (type L1) is ~195µm; and for sample 41 (type L2) is ~100µm. These measures are taken from grains that are considered representative, however punctually bigger sizes can be found, for example on SV01 ~415µm.

Type D grains are characterized by more or less straight boundaries usually forming ~45° with respect to the compression direction (σ_1). Sometimes they can also be in a horizontal disposition (*i.e.*, perpendicular to σ_1). Type D porphyroclasts−generally−present a similar grain size compared to L1 and bigger compared to L2. Samples can also present small strain free recrystallised grains nearby the mantle (*i.e.*, edge) of the larger grains. The size of the recrystallised grains in type D is smaller than in type L1 (*e.g.*, ~10µm diameter in sample SV01). Some grain
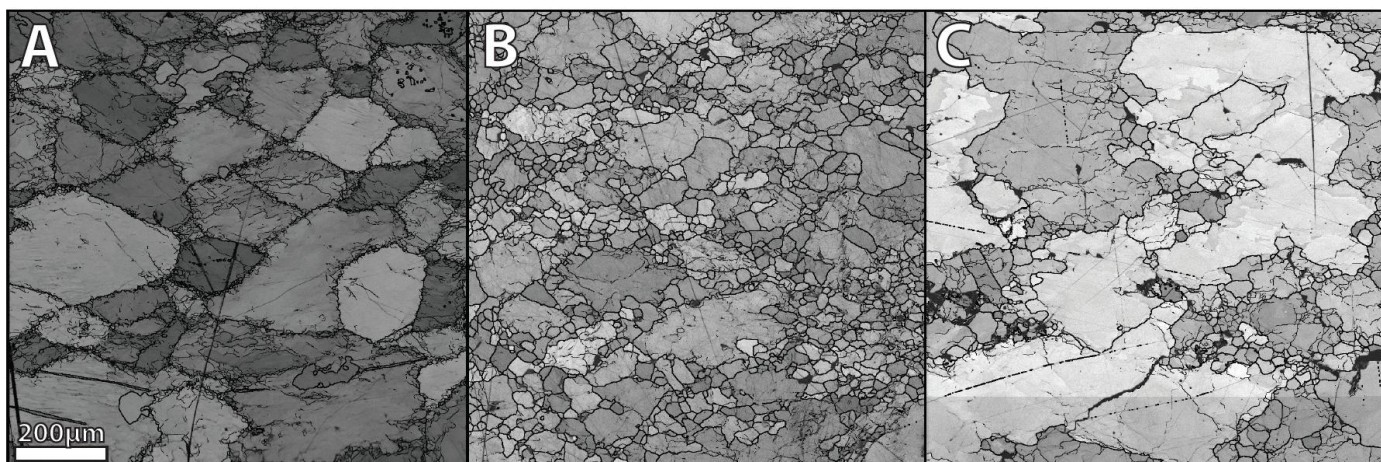
Figure 8. Examples of the general aspect of the observed microstructes: **a)** type D, sample SV01; **b)** type L1, sample 44; and **c)** type L2, sample 41. Each map is 1x1 mm and has been filtered with the Kikuchi band contrast option, which results in a gray scale map where dark colours represent low contrast. The orientation of the samples and the direction of the applied σ1 is the same for all samples. It can be observed that grains on sample SV01 present a diamond shape whereas samples 44 and 41 are more lobate. The amount and size of recrystallised grains varies in each sample.

boundaries present well defined bulges (*e.g.,* sample 29). It can also be observed that most large grains accumulate strain at the mantles forming subgrains, although sometimes big nets of dislocations can also be found at the core of the porphyroclasts. Occasionally, twins have been observed in large grains as well. Nevertheless, their abundance is not notorious.

Type L1 grains can present different grades of lobate boundaries. The general grain size of the whole sample is reduced with respect to the original undeformed microstructure (Table 4). Porphyroclasts are similar in size compared to type D but they are also more lobate. Larger grains also present nets of dislocations within them, especially at the mantle. However, the amount of subgrains seems to be minor than in diamond-shaped type microstructures. Recrystallised grains are commonly strain free and bigger in size (*e.g.,* ~100μm diameter in sample 33) compared to D and smaller than in L2 (*e.g.,* ~165μm diameter in sample 26). They are located surrounding the porphyroclasts. In this kind of microstructures twins are not present, instead necking structures can occasionally be observed (*e.g.,* sample 25).

Type L2 grains present a lower grade of lobate shapes compared to L1 but most recrystallised grains are larger in size instead (*e.g.,* up to ~480μm diameter in sample 33). The amount of recrystallised grains is reduced. Bulges are very present (*e.g.,* samples 21 and 25) as well as necking structures (*e.g.,* sample 27). Most porphyroclasts are strain free at the core and some of the mantles present dislocations. On the other hand, I can also observe areas (*e.g.,* sample 27) with high amount of subgrains.

Moreover, by plotting the PARIS factor against temperature. It can be observed a negative linear relation whereas PARIS factor against flow stress indicates a positive linear relation (Fig. 9). Thus, the plots also confirm an inverse relationship between temperature and stress. In Figure 4a type D and type L1 miscrostructures are concentrated
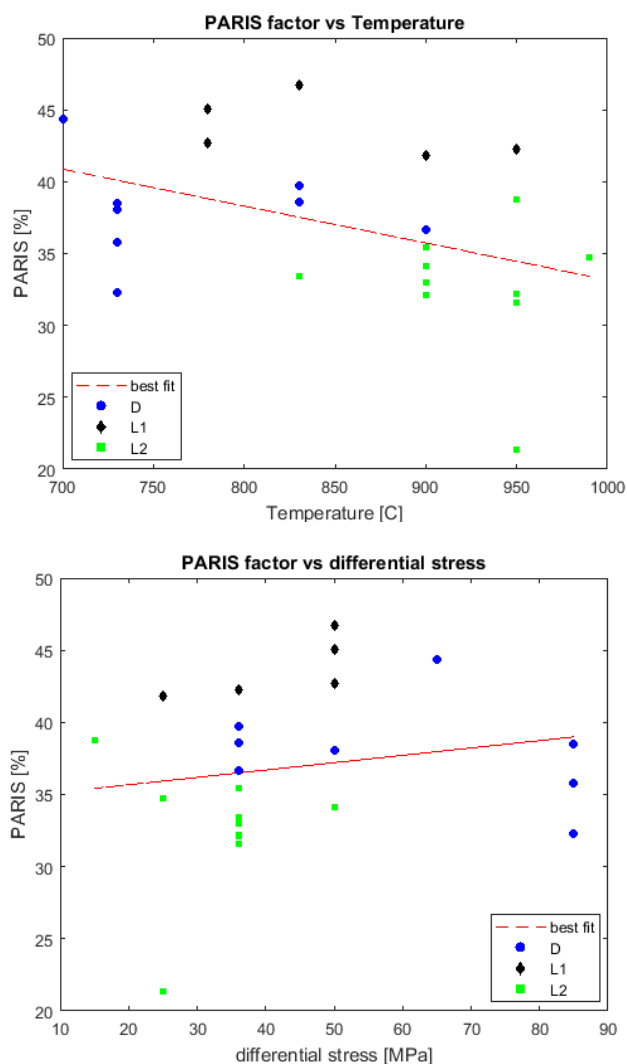
Figure 9. upper) PARIS against temperature plot; and **lower)** PARIS against differential stress plot. The former presents a negative linear relation ($R^2 = 0.1648$) whereas the latter shows a positive trend ($R^2 = 0.0305$). Blue dots symbols indicate D (diamond shaped); black diamond indicate L1 (lobate with small porphyroclasts); and green squares indicate L2 (lobate with larger porphyroclasts). The respective values of R^2 are relatively low. In the upper plot it can be observed that diamond shaped microstructures are located at lower temperatures with respect to lobate ones. On the contrary, type D microstructures present higher differential stresses.

mostly at low/high-intermediate T−high PARIS values whereas L2 microstructures are concentrated at high T−low PARIS values. Type L1 microstructures tends to be at slightly higher T (780−950ºC) than type D (700−900ºC). L2 microstructures are located at temperatures ranging 900−1000ºC. The plot between PARIS and flow stress indicates that type D miscrostructures are concentrated mostly at intermediate−high σ and

high PARIS values whereas type L1 and L2 microstructures are concentrated at low/low−intermediate σ and low PARIS values. L2 microstructures tend to be located at slightly lower σ (15−50 MPa) than type L1 (25−50 MPa). Type D are located at flow stresses between 35−90 MPa.

2.6 Pole figures

Pole figures (PF) show a strong CPO for the projection on the $c(0001)$ plane. It can be observed that there are three main textural distributions. The first configuration (Fig. 10A) presents strong one/two point maxima clusters of [c]-axes parallel to σ_1 (*i.e.,* N−S). The second configuration (Fig. 10B) can be found but forming a girdle distribution instead of clusters. The third configuration (Fig. 10C) implies clusters and/or girdles which are not parallel to σ_1, generally randomly located in the inner area of the stereogram.

For strong bipoles parallel to σ_1 in $c(0001)$, the f slip planes show maximum girdle distributed E−W

more dispersed but still evidences a clear CPO. For distributions not parallel to σ_1 in $c(0001)$, pole distributions in f do not show an E−W configuration but are dispersed randomly along the plot.

Regarding to the quantitative analysis of CPO strength and shape, Table 6 collects the numerical results of the J-index; M-index; C-index; K-index, and its decomposition on $\ln(\lambda1/\lambda2)$ (cluster distribution component) and $\ln(\lambda2/\lambda3)$ (girdle distribution component); and PGR values.

Firstly it can be observed that the values for J-index are relatively low, with a maximum of 14.69 for sample 41 and a minimum of 2.03 for sample 40. Values for M-index are also relatively low, with a maximum of 0.29 for sample 25 and a minimum of 0.01 for sample 40.

On the other hand, Figure 11 illustrates the $\ln(E1/E2)$ vs $\ln(E2/E3)$ plot proposed by Woodcock (1987). It can be observed that pole figures with well-defined clusters are located closest to the $\ln(E1/E2)$ whereas girdle-like distributions have
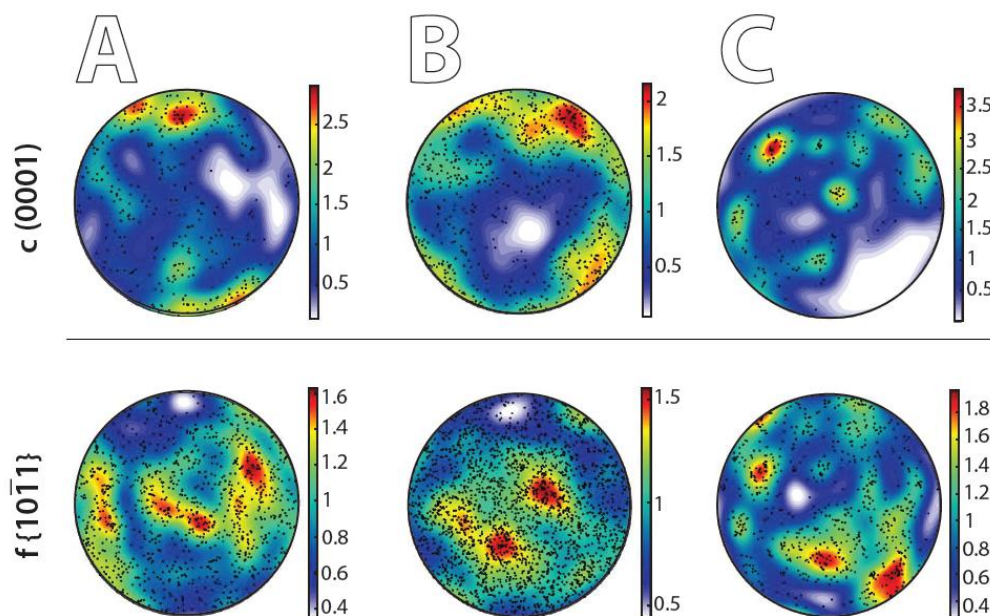
Figure 10. Representative pole figures for each type of defined microstructuree: **a)** D, sample SV01; **b)** L1, sample 44; and **c)** L2, sample 41. As it can be observed for the $c(0001)$ plane, each sample presents a different CPO distribution: **a)** [c]-axis forming clusters parallel to the compression direction (located at the North); **b)** [c]-axis forming girdles parallel to the compression direction; and **c)** random distributed poles.

parallel to X. If girdles are present instead of clusters in $c(0001)$, the E−W distribution in f is

highest $\ln(E2/E3)$ values.

Table 6. Values for quantitative analysis of CPO strength

sample	J	M	C	K	ln(E1/E2)	ln(E2/E3)	P [100%]	G [100%]	R 100%
40	2,03	0,01	0,25	0,72	0,10	0,14	3,67	9,02	87,31
35	2,52	0,02	0,43	3,48	0,34	0,10	12,04	5,55	82,41
29	3,02	0,02	0,52	0,50	0,17	0,35	6,50	20,21	73,29
43	3,08	0,03	0,64	1,10	0,33	0,30	12,68	16,73	70,59
33	2,72	0,03	0,86	0,84	0,39	0,47	15,51	24,03	60,46
31	4,47	0,04	0,71	0,79	0,31	0,40	12,14	21,68	66,18
24_2a	5,42	0,04	0,59	3,73	0,46	0,12	17,03	6,74	76,23
44	2,36	0,04	0,88	0,70	0,36	0,52	14,42	26,75	58,83
37	2,34	0,05	0,84	1,85	0,54	0,29	20,78	14,65	64,57
22	4,25	0,05	0,96	1,73	0,61	0,35	23,58	16,75	59,67
21	4,61	0,07	0,91	0,98	0,45	0,46	17,76	23,08	59,16
34_1	2,80	0,07	1,16	0,80	0,52	0,64	21,12	29,70	49,18
SV02	3,35	0,08	1,25	0,91	0,60	0,65	24,43	28,79	46,78
SV05	10,00	0,11	0,96	0,37	0,26	0,70	10,64	36,23	53,13
SV01	5,03	0,12	1,45	1,48	0,87	0,59	35,05	22,51	42,43
27	12,45	0,16	1,56	1,60	0,96	0,60	38,82	21,74	39,44
34_2	3,92	0,17	1,44	5,27	1,21	0,23	45,87	7,98	46,15
41	14,69	0,18	2,08	0,26	0,43	1,66	19,49	59,46	21,05
25	9,68	0,29	1,95	18,35	1,85	0,10	64,87	2,32	32,81
26	4,03	0,04	0,70	0,30	0,16	0,54	6,42	30,13	63,45
28	3,47	0,02	0,59	0,16	0,08	0,51	3,15	29,64	67,21
sv03	2,55	0,02	0,50	9,63	0,45	0,05	16,31	2,61	81,08
sv04	3,29	0,03	0,66	1,03	0,34	0,33	12,86	17,83	69,31

Furthermore, additional stress and temperature information is given by different shape and colour respectively. It can be observed that there is a slight stress distribution pattern whereas it is not so evident on temperature. Therefore, for low flow stresses (15–25 MPa) there is a high girdle component, ranging between 0.4 to ~1.7, and a low cluster component from ~0.2 to ~0.4. For medium flow stresses (36–50 MPa) the girdle component is reduced from ~0.1 to ~0.65 whereas the cluster component increases from ~0 to ~1.8. Finally, for high flow stresses (65–85 MPa) both girdle and cluster components are reduced, from ~0 to 0.6 and ~0.3 to ~0.85 respectively. On the other hand, there are two temperature ranges, from 700–780ºC and 830–990ºC, that increase gradually from the origin towards high ln($\lambda 1/\lambda 2$) and ln($\lambda 2/\lambda 3$) values.

Finally, by plotting P, G, and R data in a triangular diagram (Fig. 12) it can be observed that most data

falls in the random field. Samples 25 and 41 are the most differentiated from this trend. Results are in agreement with those values calculated with the J-index and M-index.

2.7 Inverse pole figures

The IPF projection on EBSD maps indicates that for the Y direction there is a predominant crystallographic alignment towards the area nearby {e}, with two samples (*i.e.*, 25 and 34[1]) with strong maximum on (*c*). Other samples show a crystallographic alignment towards the area nearby {f} (*e.g.*, SV05), <*a*> (*e.g.*, 21), {r} (*e.g.*, 44), or to none of them (*e.g.*, 24, 29 or 31) (Fig. 13). In addition, most samples present only one maximum, a few samples present more than a maximum (*i.e.*, 29, 34[2], 40, and 44).
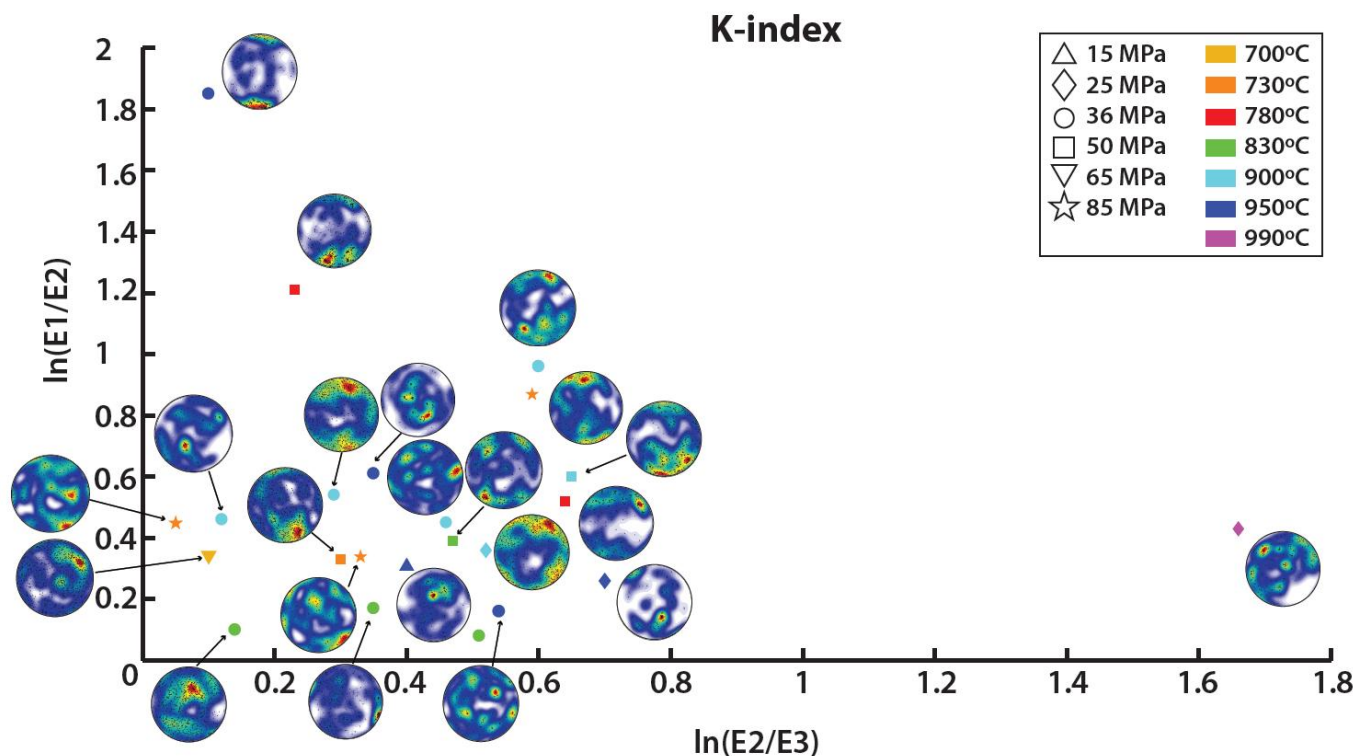
Figure 11. Plot based on the one proposed by Woodcock (1987). Ideally, points located nearby the origin are indicative of dispersed values/weaker CPOs whereas higher $\ln(\lambda2/\lambda3)$ or $\ln(\lambda1/\lambda2)$ indicate concentrated values/strong CPOs. Points located at low $\ln(\lambda1/\lambda2)$ present girdle distributions and they evolve to clusters with increasing $\ln(E1/E2)$ values. It can be observed that my points are in agreement with the model at some points (*e.g.,* samples 25, 34_2 and 41) but they differ especially near the origin (*e.g.*, samples 40, 29 or 31). Stress and temperature values have been introduced by different shapes and colors, respectively. The plot reveals that there is a better stress distribution than temperature one. Low stresses have higher $\ln(\lambda2/\lambda3)$ and lower $\ln(\lambda1/\lambda2)$; medium stresses have medium $\ln(\lambda2/\lambda3)$ values and variable $\ln(\lambda1/\lambda2)$; whereas higher stresses have low $\ln(\lambda2/\lambda3)$ and high $\ln(\lambda1/\lambda2)$. On the other hand there is temperature increment from the origin towards high $\ln(\lambda2/\lambda3)$ and $\ln(\lambda1/\lambda2)$ in two ranges, 700 to 780°C and 830 to 990°C.

2.7.1 *Intragranular misorientation of subgrains*

The results indicate that the rotation axis (*i.e.,* misorientation axis) is in general preferentially parallel to (*c*), {*f*}, {*m*} and <*a*>. The distribution appears in several different patterns. Therefore, for CPO with strong one/two point maxima clusters parallel to σ_1 there is a maximum parallel to <*a*> and a strong alignment towards {*m*} and {*f*} (Fig. 14A). On the other hand, for CPO with girdles parallel to σ_1 there is no alignment with <*a*>, thus maximum alignment is towards {*m*} and {*f*} and in some samples (*c*) becomes more important (Fig. 14B). Finally, for random CPO there are two different possibilities, misorientation axes can be parallel to (*c*) or to {*f*} and {*m*} (Fig. 14C).
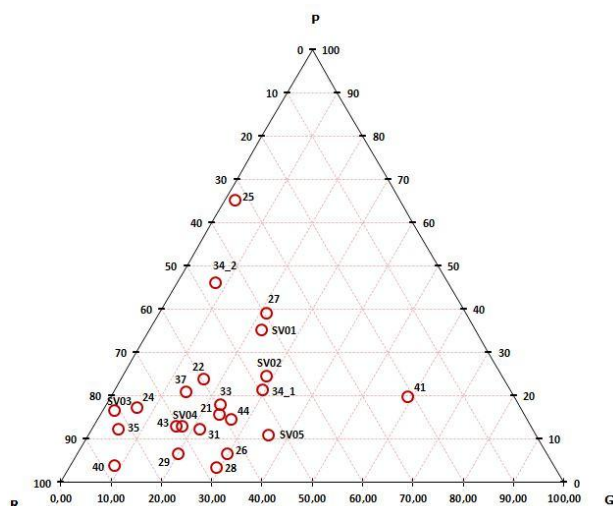
Figure 12. Triangular diagram based on the one proposed by Vollmer (1990). P refers to point, G to girdle, and R to random. It can be observed that most samples are located within the random field. Samples 25 and 41 are the most differentiated ones, falling in the point and girdle fields respectively.
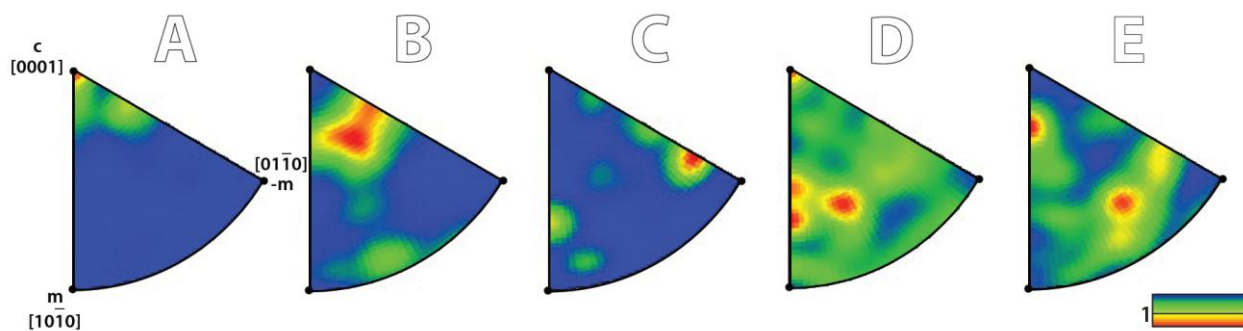
Figure 13. Collection of the most representative Y-IPF projections: **a)** sample 25; **b)** sample SV01; **c)** sample SV05; **d)** sample 44; and **e)** sample 29. It can be observed that several configurations can be obtained, without one concrete being dominant.

Furthermore, I have determinate the direction of the direction of the misorientationaxesofsubgrain boundaries for each slip systemfor both tilt and twist boundary (Table 7). No twist boundaries have been determined for misorientationaxes parallel to <*a*>since there is no appropriate screw dislocation of this type in calcite (Bestmann and Prior, 2003).

2.8 Schmid factor

By comparing the SF maps for each type of CPO distribution (Fig. 15) it can be noticed that there is a shift in predominant slip system activity. In addition, several slip systems can be operative within a single grain whereas in other cases one single slip system is restricted to a determinate microstructural feature, for instance, twins.

Therefore, for CPO with strong one/two point maxima clusters parallel to $\sigma 1$ all slip systems are active, with fewer activity on the *c* slip system (Fig. 15A), as it can be observed for the low SF values. On the other hand, for CPO with girdles parallel to $\sigma 1$ {*f*} <2-201> (*i.e.*, low temperature regime) is less active than for high temperature regime. In addition, *c* slip system is less favourable to slip than {f} <10-11> since more grains do not reach the CRSS for slip (Fig. 15B). Finally, for random CPO {*f*} <2-201> is still less favourable for slip than {f} <10-11>. However, unlike the previous case, slip on c is more favourable than slip on {f}<10-11> (Fig. 15C).

Furthermore, Table 5 collects the values for CRRS and the corresponding minimum SF. It can be observed that in most samples SF is high enough to allow slip in most grains. A big exception is sample 31, where no grains can slip on {f}<2-201>.
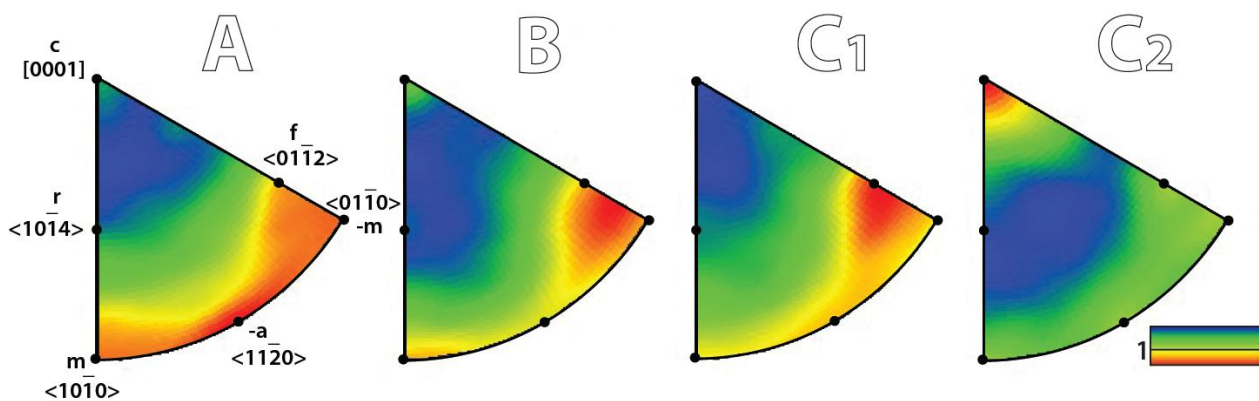
Figure 14. IPF for misorientation axes of subgrain boundaries for each type of defined microstructure: **a)** D, sample SV01; **b)** L1, sample 44; **c1)** L2, sample 41; and **c2)** L2, sample 21. It can be observed that there is a gradual change along the different type of microstructures on the alignment of misortientation axes with respect to the crystallographic reference. This triangle corresponds to the unit cell indicated in Figure 1.

Table 7. Recompilation of tilt and twist boundaries for the predicted active slip systems

		Misorientation axes of subgrain boundaries	
Slip systems		**Tilt boundary (Edge dislocation)**	**Twist boundary (Screw dislocation)**
c (0001)<-12-10>		<10-10>	[0001]
LT	**f{-1012}<2-201>**	<12-33>	<-1012> + [0001]
HT	**f{-1012}<10-11>**	<-12-10>	<-1012> + [0001]
m {10-10}<-12-10>		[0001]	<10-10> + [0001]
a{-12-10}<-2021>		<10-14>or <-1012>	-
r{10-14}<-2021>		<-12-10>	<10-14>+ [0001]
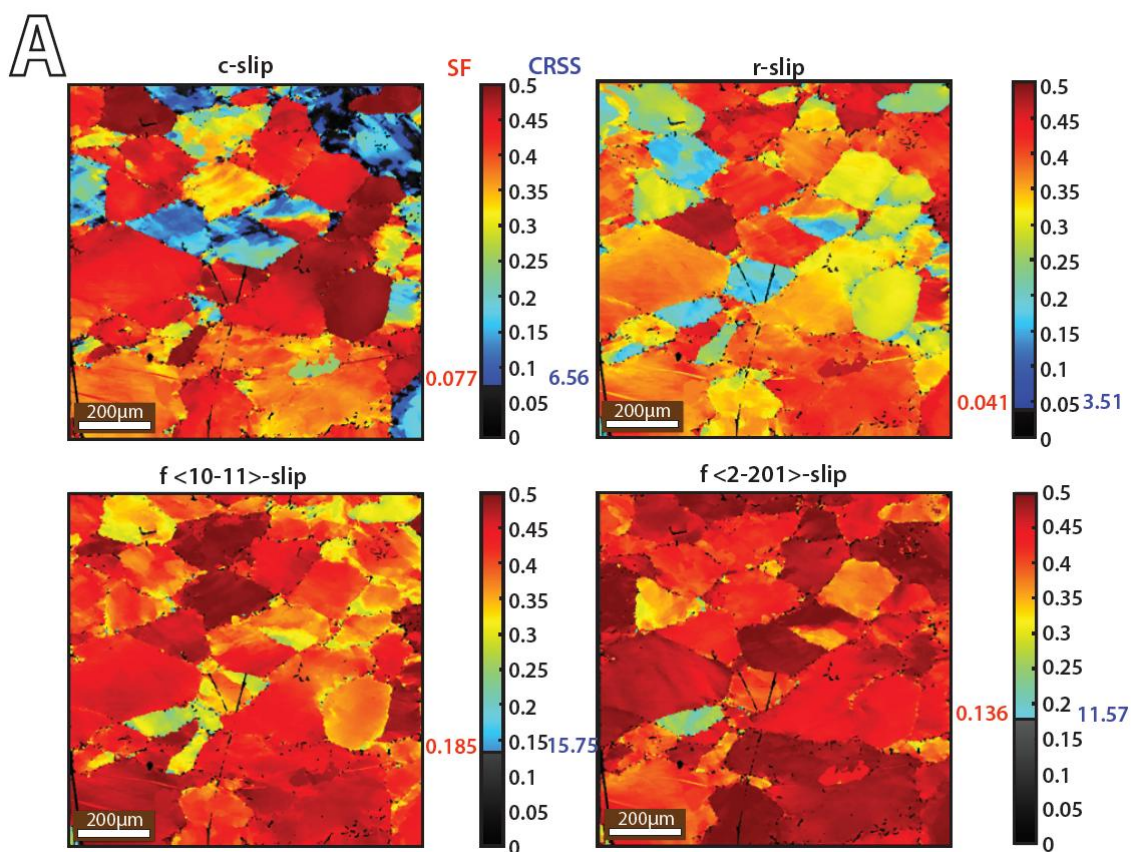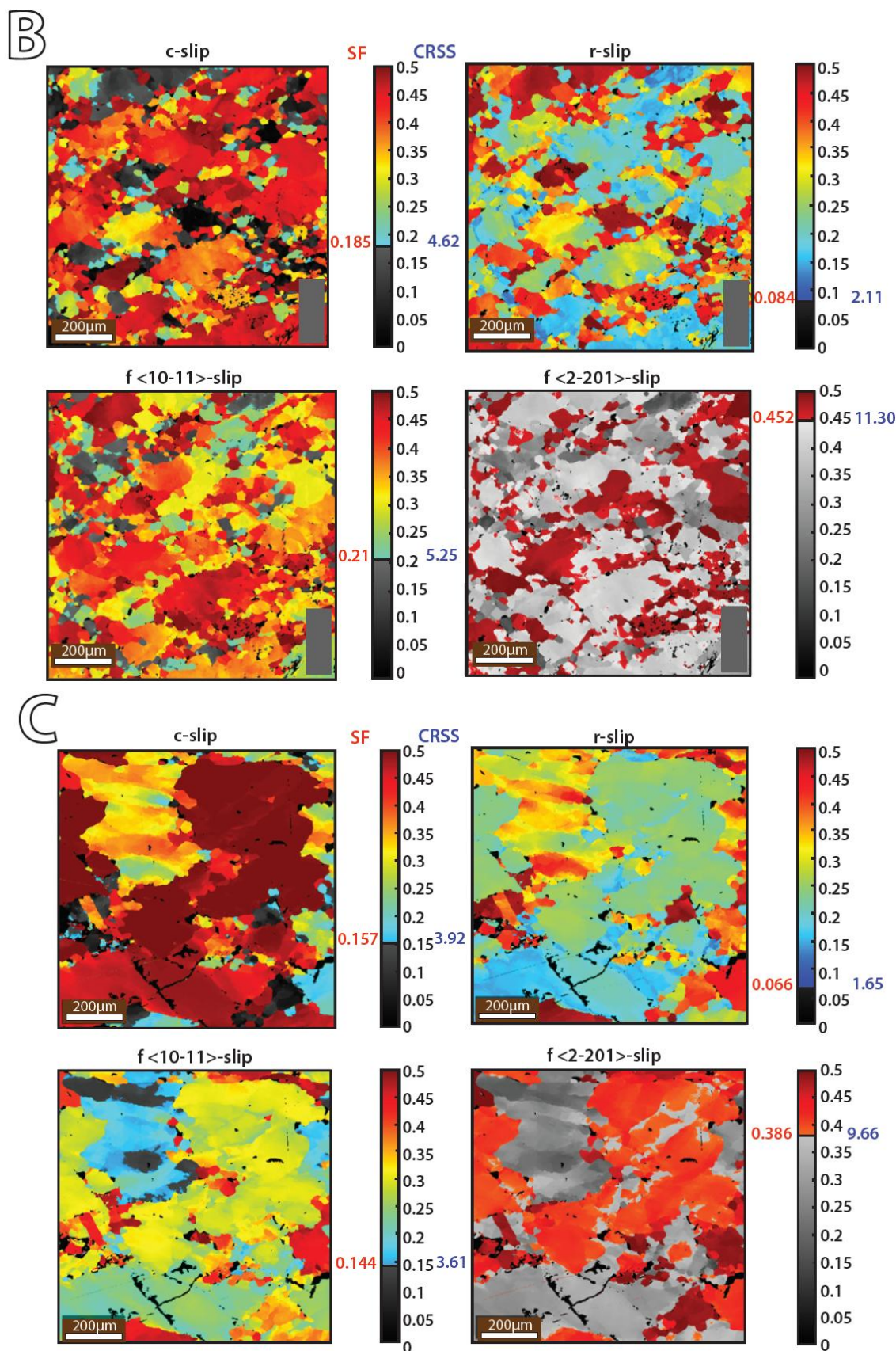
Figure 15. Schmid Factor maps for: **a)** D, sample SV01; **b)** L1, sample 44; and **c)** L2, sample 41. We find out that for diamond shape grains all slip systems are in a good orientation for slip, especially {*f*} as indicated by warm colors (*i.e.*, high SF). Nevertheless, (*c*) presents some hard orientations as indicated by blue colors (*i.e.*, low SF). For lobate grains, with girdle CPO we can observe that the minimum SF has increased. In this case, the {*f*}<2-201> (low T regime) requires more stress to slip, and {*f*}<10-11> (high T regime) is more likely to slip than (*c*). For lobate grains with random CPO, {*f*}<2-201> is still poorly favour to slip. However, (*c*) is more likely to slip than {*f*}<10-11>.

4. DISCUSSION

The approach of the present project is to determine if evolving recrystallisation mechanisms do have an impact on CPO patterns during changing experimental conditions and, if so, how can these patterns be developed into a model which can be used on natural samples. For this purpose, I conducted EBSD analysis by using CHANNEL 5 and MTEX. Oncoming sections deal with the discussion of the obtained results by micostructural characterization, (inverse) pole figures, inverse pole figures of misorientation axis of subgrain boundaries, and Schmid factor. As a result, I aim to contribute to a better understanding of the impact of dynamic recrystallisation on the general geodynamic picture.

4.1 Separating the recrystallised fraction

On light of the results (Fig. 8), it seems that both porphyroclasts and recrystallised fractions have been affected by the same deformation mechanisms and because of that, the oncoming arguments will be referred to both fractions. I consider though, that even if the results may not change, the methodology applied in this study to separate both fractions can be further improved. In this train of thought I consider that MTEX analysis can provide better results than Channel 5–the latter being the software used in this work. I consider that Channel 5 does not provide enough tools to provide a satisfactory discrimination of the grain size distribution. Moreover, the difficulty of defining appropriate criteria to separate both subfractions has represented a setback, preventing us of using MTEX for this purpose.

4.2 Microstructures and PARIS factor

My results (Fig. 8) stablish a transition between angular/ diamond-shaped to lobate grains with increasing temperature and/or decreasing stress. This is in accordance with classical models (Drury and Urai, 1990; Hirth and Tullis, 1992; Passchier and Trouw, 2005). From the morphology I have infer that diamond shaped grains are formed by dislocation-accommodated grain boundary sliding (disGBS), where strain is accumulated at the grain boundaries and/or triple junctions (Drury and Humphreys, 1988; Drury and Urai, 1990; Hansen *et al*., 2011) (Fig. 16). Excess in strain is removed by dislocation motion, by two different recrystallization mechanisms: subgrain rotation (SGR) and grain boundary migration (GBM) (Fig. 16). It can be observed that changes in grain morphology are followed by a transition in the recovery mechanisms. Therefore SGR is dominant in diamond shaped grains whereas GBM is dominant in lobate grains. However, it can also be inferred that minor GBM is active in diamond-shape grains as bulging can be also found at the grain boundaries (Drury *et al.*, 1989).

A footnote should be added at this point since I am considering the microstructural description of the samples. I used the PARIS factor in order to separate diamond shaped grains from lobate grains as an attempt to relate more accurately the relation between the shape (taken as indicator of the predominant recrystallisation mechanism) and the temperature or flow stress conditions. Therefore, I expected low PARIS factor for angular grains and increasing values towards lobate grains. However, Table 4 contradicts this prediction since there is not a clear distinction between both microstructures. In addition, I expected to find a positive linear correlation between the average PARISof each sample and T and a negative linear correlation between PARIS and differential stress. This would have indicated that more lobate shapes are formed at HT-Lσ whereas angular shapes would have developed preferentially in LT-Hσ conditions. This is not in accordance with the result obtained in Figure 9. At this point one must consider if the applied grain shape descriptor is accurate enough or rather the initial hypothesis of LT-Hσ conditions for angular grains and/or HT-Lσ for lobate grains is just not as initially expected.

Heilbronner and Barret (2014) argued that PARIS factor is insensitive to the grain shape and so the variability of its values depends only of the "excess of projection", which is expressed as ΔP in Figure 17A. This would make PARIS a bad grain shape descriptor for my purpose, since angular grains present high degree of bulging at the grain boundaries, increasing the PARIS value to similar to those for lobate grains.

A possible alternative that I now take into consideration would be to calculate and combine information related to the area and the perimeter of the grains (Fig. 17B). In case that the results proved a better shape differentiation I could further proceed to relate the shape descriptor with T and stress. Mathematically, the new shape descriptors are described as:

$$deltP = \frac{\Delta P}{P} \cdot 100\% \qquad (18)$$

$$deltA = \frac{\Delta A}{A} \cdot 100\% \qquad (19)$$

$$radius\Delta = \sqrt{deltA^2 + deltP^2} \qquad (20)$$

Nevertheless, since final discernment of microstructures were done visually I consider that the presented type D, L1 and L2 division is reasonable good. The accuracy of the trends from Figure 9 should be double checked by applying a different shape descriptor.

Nevertheless, I consider that I can still use the data obtained from the PARIS factor. I have calculated the amount of fully convex grains (*i.e.,* PARIS factor =0%) and plotted it against the amount of grains of the sample and the total average PARIS factor (Fig. 18). It can be observed that type D has the largest amount of grains in the sample whereas L2 presents the lowest amount. Furthermore, type L1 has the minimum amount of PARIS values equal 0% whereas type D has the largest amount. Consequently, I infer that relative similar PARIS values between type L1 and D are due to an equilibrium between large amount of grains for type D and L1 and large amount of convex grains for type D. Besides, low PARIS on L2 is due to a lower amount of grains and high amount of convex shapes.

I infer that the maximum values for convex grains is caused by the formation of recrystallised grains, which is in accordance with the high amount of
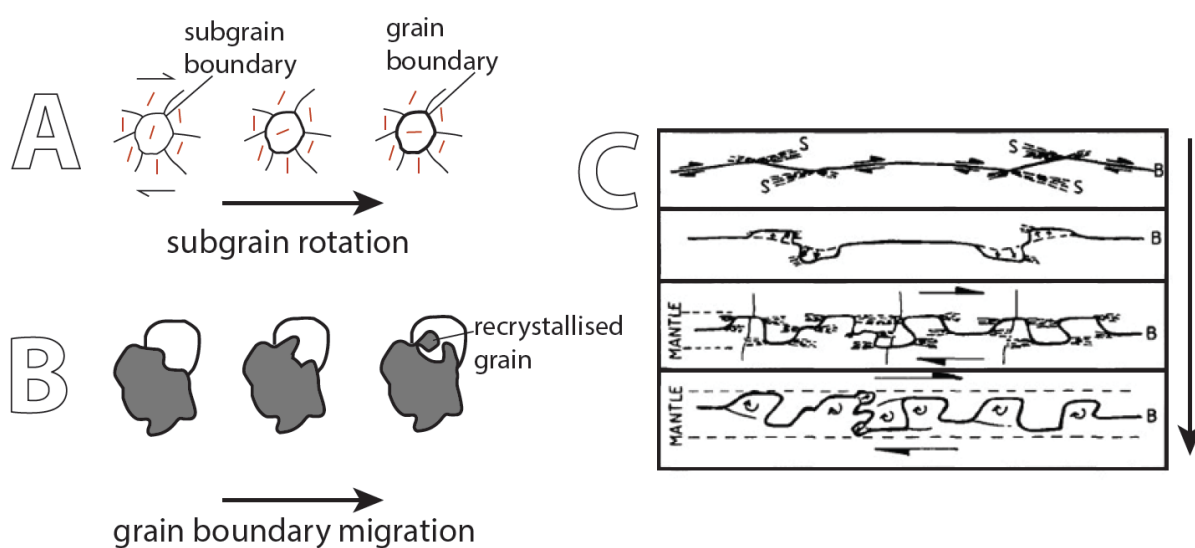
Figure 16. Conceptual model of: **a)** SGR; and **b)** GBM (Valcke, 2008) and **c)** GBS (Drury and Humphreys, 1988). SGR involves the formation of new grain boundaries whereas GBM involves the migration of already existing grain boundaries (Drury and Urai, 1990). GBS causes high strain accumulation at the grain mantle triggering boundary migration and forming bulges. Bulging (BLG) is considered to be a combination of SGR and GBM, the former acting first (Valke, 2008).
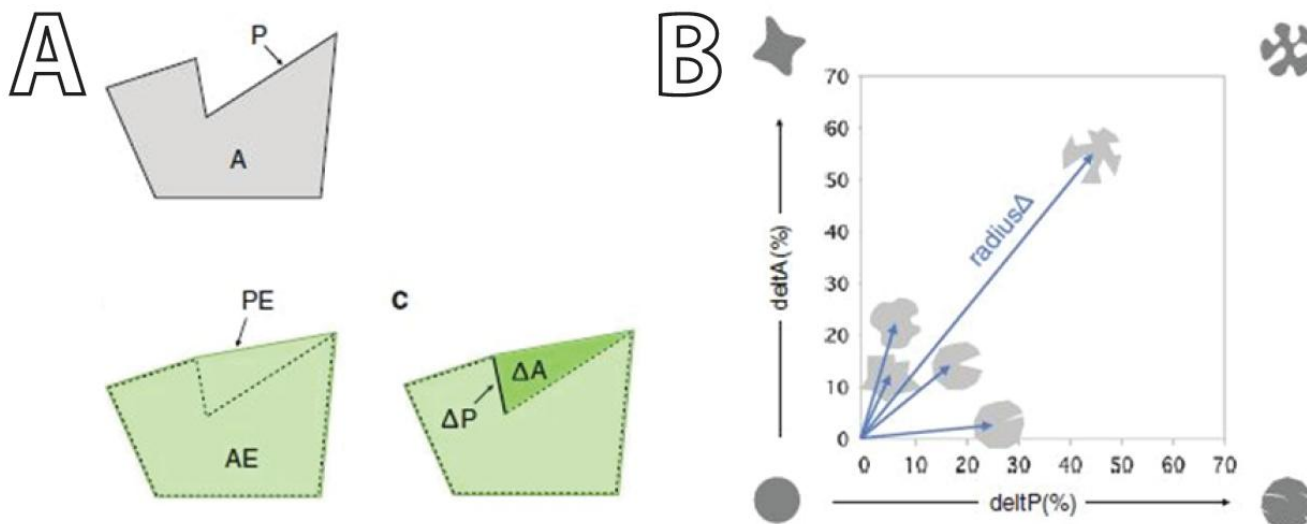
Figure 17. a) Shape descriptors derived from the presence of a convex hull (PE)**,** ΔP is the excess of projection and it constitutes the parameter which PARIS is sensitive to**;** and **b)** diagram obtained from the projection of both shape descriptors deltA and deltP (Heilbronner and Barret, 2014), I consider that this might be a better alternative to the use of the PARIS factor.

grains in samples from type D. Minimum amount of 0% values present in type L1would reflect a higher activity of GBM. Moreover, I infer that the higher amount of grains in type L1 samples could be either be represent an early stage of GBM (*e.g.,* sample 44), which would imply high amount previous recrystallised grains, or because of a larger amount of disectionated grains generated by GBM (*e.g.,* sample 34_2).

4.3 Pole figures and quantification of CPO strength

In order to compare my CPOs to previous models (*i.e.*, Qi *et al*., 2017 on ice) I have organized $c(0001)$ and $\{f\}$<10-11> pole figures by decreasing flow stress (Fig. 19), since Qi *et al*., 2017 did not consider temperature variations on their experiments. I have divided the pole figures in three subsets: high (85 to 65 MPa); medium (50 MPa); and low (36 to 15 MPa) flow stress.

It can be observed in the $c(0001)$ plane that for high flow stresses only one sample (SV01) presents $[c]$-axis maximum parallel to σ_1. I infer that high strains (0.45 or above) are necessary, since samples SV03 and SV04 were deformed at same temperature and flow stress conditions but less strain giving as a result random distributions of the maximum clusters.

For flow stresses of 50 MPa, there is one single sample (43) with a $[c]$-axis maximum parallel to σ_1. Samples 34_1 and 34_2 present a similar configuration but the clusters are slightly more girdled. On the other hand, samples SV02 and 33 present well developed girdles also parallel to σ_1. Consequently, from his subset I can infer that lower temperatures cluster maximums parallel to σ_1 whereas with increasing temperature they become more girdled.

Besides, for low flow stresses I can find both previous configurations plus stronger/weaker clusters randomly distributed within the projection. Samples 25 and 37 show $[c]$-axis maximum parallel to σ_1. Sample 27, 40 and 44 presents girdles whereas samples 26, 22, 24 and 21 present random orientations. I infer that random distributions are due to low strain conditions (below 0.45) whereas samples 27, 40 and 44 are girdled because temperature are not high enough (below 950°C) at the present stress.

For pole distributions on the $\{f\}$<10-11> projection It can be observed a correspondence but represented as stronger/weaker E–W girdles.
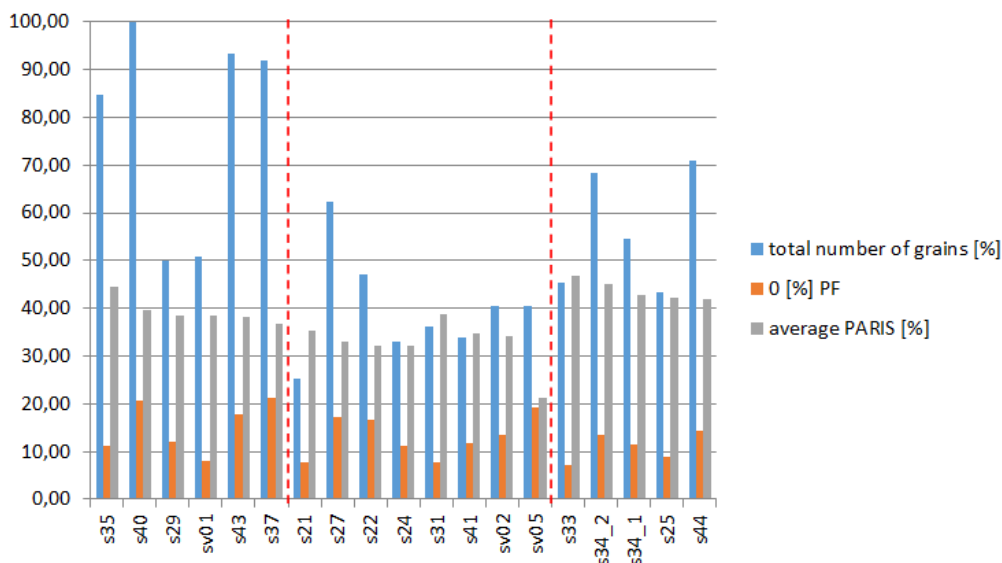
Figure 18. Diagram comparing the average PARIS for each sample, the total amount of grains and the number of grains with 0% value for PARIS. It can be observed that type D microstructures have the largest amount of grains and 0% PARIS values followed by L1 and then L2. I infer that this is the main reason for the similitude of PARIS values between type D and L1. Red dashed line separates type D, L2, and L1 microstructures, respectively.

As a general approximation, I can define that [c]-axis maximum parallel to σ_1 are formed when $\varepsilon \geq 0.45$, preferably at high stress–low temperature conditions (except for sample 25). Girdles are formed with increasing temperature/ decreasing stress and/or at $\varepsilon = 0.45$. Random orientations are presumably more abundant when $\varepsilon < 0.45$, preferably at low flow stress and high temperature conditions.

Furthermore, data acquired qualitatively (Table 6) indicates weak CPOs for my samples, except for sample 25. Thus, as it can be seen in Figure 19, most samples fall in the random domain. However, the projection of PF indicates that some of the samples quantified as random present strong clusters or girdles as a reflection of a marked CPO. Contradictory results similar to ours were reported by Hansen *et al*. (2011) for olivine, where they obtained very low M-index values (0.042 to 0.054) and strong CPOs projections with clusters parallel to the compression direction. Hansen *et al*. (2011) argued that these results were consistent if considering the magnitude of applied effective strain over the samples (~18%). Qi *et al*. (2017) also reported random values for M-index at low strain conditions. Therefore, I consider that the

reported values might not be incorrect, although I do not preclude a minimal percentage of error.

On the other hand, Figure 11 does not perfectly match with the theoretical model designed by Woodcock (1977), where spread pole projection are concentrated nearby the origin whereas concentrated pole values are higher at large ln(E1/E2) or ln(E2/E3) values. However, Figure 11 does a relatively good distinction of major distributions which are in agreement with Woodcocks model, with cluster configurations for large ln(E1/E2) and girdles for ln(E2/E3) values. In addition, it seems that K-index reflects a better pattern for flow stress rather than temperature.

4.4 Intragranular misorientation axis and Schmid factor

Based on Figure 19, it can be observed a distribution of misorientation axis projections of

A

SV01

PARIS: 38.45 % (D)
$\Delta\sigma$/ T/ ε: 85 MPa /
730°C / 0.45
$\dot{\varepsilon}$: -

(0001)

{10$\bar{1}$1}
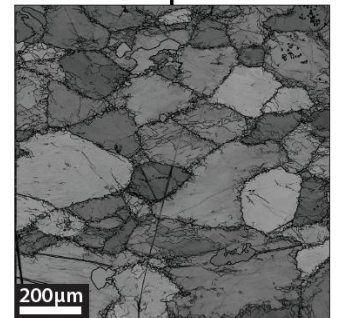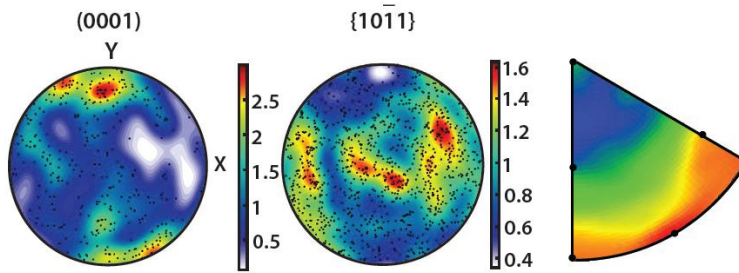
SV03

PARIS: 35.78% (D)
$\Delta\sigma$/ T/ ε: 85 MPa /
730°C / 0.3
$\dot{\varepsilon}$: -
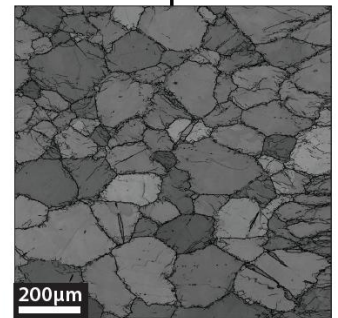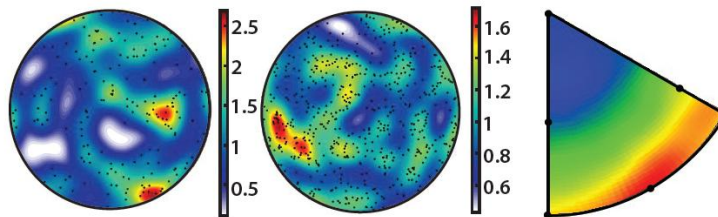
SV04

PARIS: 32.25 % (D)
$\Delta\sigma$/ T/ ε: 85 MPa /
730°C / 0.15
$\dot{\varepsilon}$: -

35

PARIS: 44.38 % (D)
$\Delta\sigma$/ T/ ε: 65 MPa /
700°C / 0.45
$\dot{\varepsilon}$: 3.8*10^{-6} s^{-1}

c
[0001]

f
<01$\bar{1}$2>

r
<10$\bar{1}$4>

-m
<01$\bar{1}$0>

-a
<11$\bar{2}$0>

m
<10$\bar{1}$0>

decreasing
flow stress

200μm
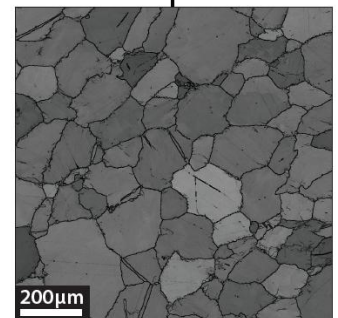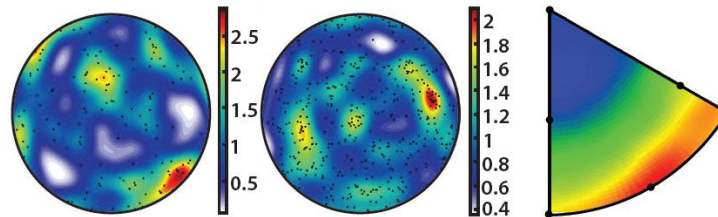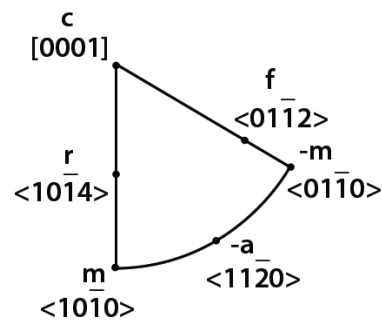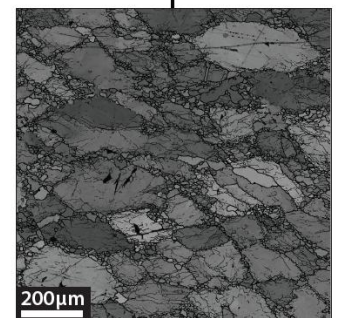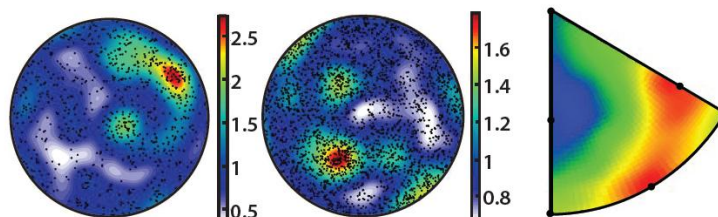
B

SV02
PARIS: 34.14 % (L2)
$\Delta\sigma$/ T/ ε: 50 MPa /
900°C / 0.45
$\dot\varepsilon$: –

(0001) {10$\bar{1}$1}
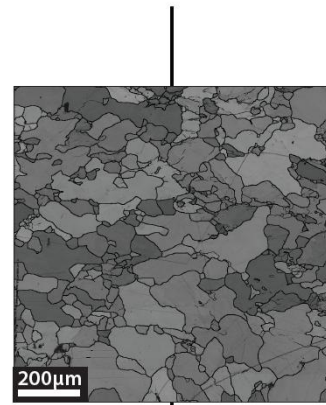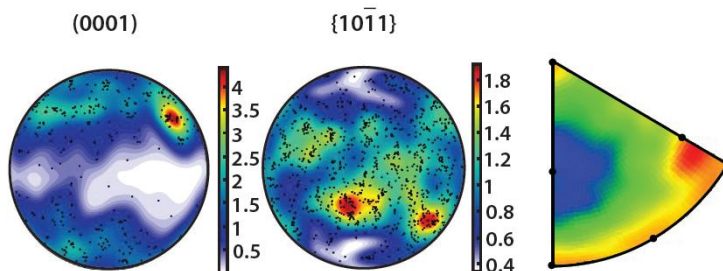
33
PARIS: 46.72 % (L1)
$\Delta\sigma$/ T/ ε: 50 MPa /
830°C / 0.45
$\dot\varepsilon$: 4.7*10^{-4}s^{-1}
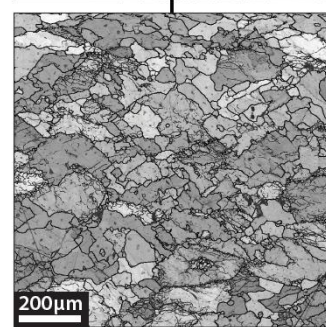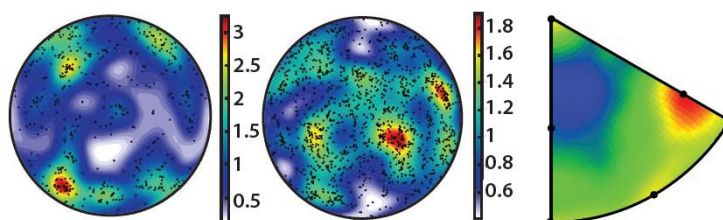
34$_2$
PARIS: 45.06 % (L1)
$\Delta\sigma$/ T/ ε: 50 MPa /
780°C / 0.45
$\dot\varepsilon$: 4.7*10^{-5}s^{-1}
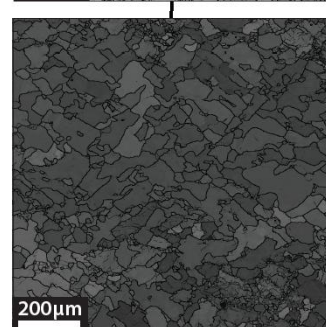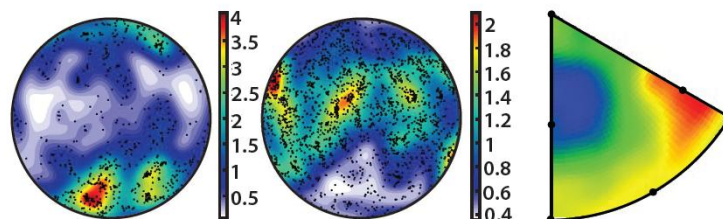
34$_1$
PARIS: 44.38 % (L1)
$\Delta\sigma$/ T/ ε: 50 MPa /
780°C / 0.45
$\dot\varepsilon$: 4.7*10^{-5} s^{-1}
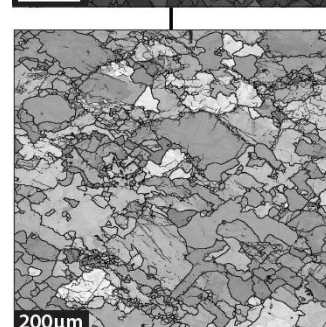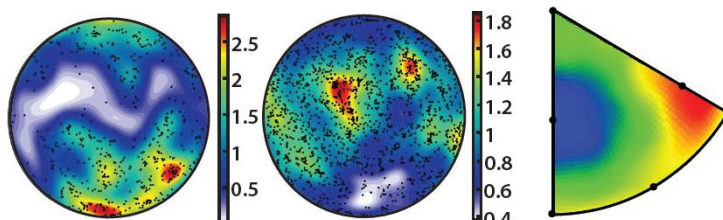
43
PARIS: 38.07 % (D)
$\Delta\sigma$/ T/ ε: 50 MPa /
730°C / 0.45
$\dot\varepsilon$: 3.9*10^{-6}s^{-1}

200μm

decreassing
flow stress

(0001)   {10$\bar{1}$1}
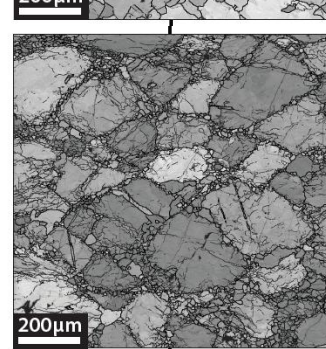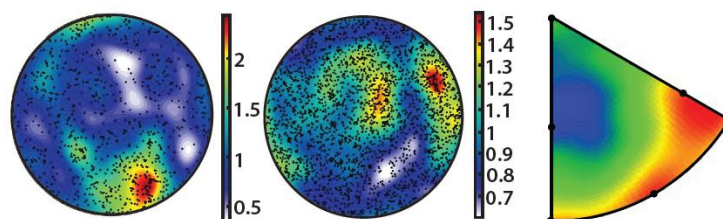
25
PARIS: 42.69 % (L1)
$\Delta\sigma$/ T/ ε: 36 MPa /
950°C / 0.45
$\dot{\varepsilon}$: -
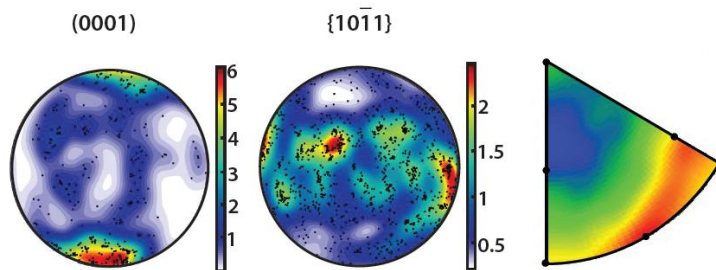
26
PARIS: 31.55 % (L2)
$\Delta\sigma$/ T/ ε: 36 MPa /
950°C / 0.3
$\dot{\varepsilon}$: -
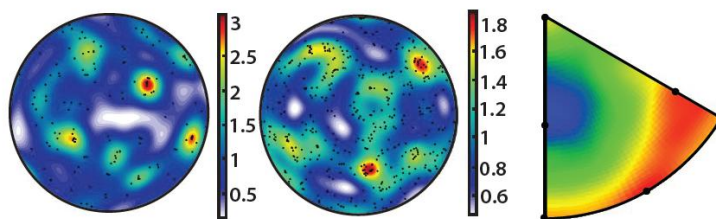
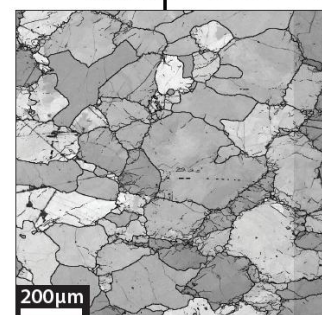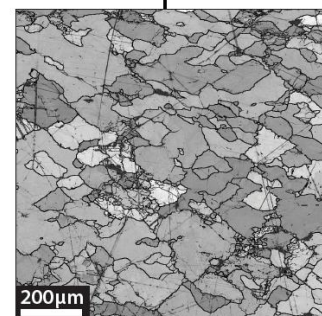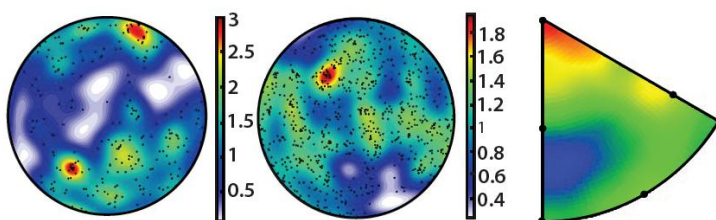**22**
PARIS: 32.2 % (L2)
$\Delta\sigma$/ T/ ε: 36 MPa /
950°C / 0.15
$\dot{\varepsilon}$: 4.2*10^{-6} s^{-1}
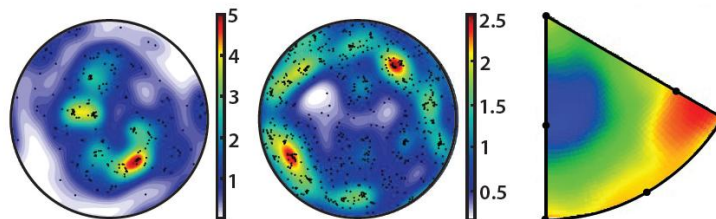
37
PARIS: 36.66 % (D)
$\Delta\sigma$/ T/ ε: 36 MPa /
900°C / 0.9
$\dot{\varepsilon}$: 7.1*10^{-5} s^{-1}
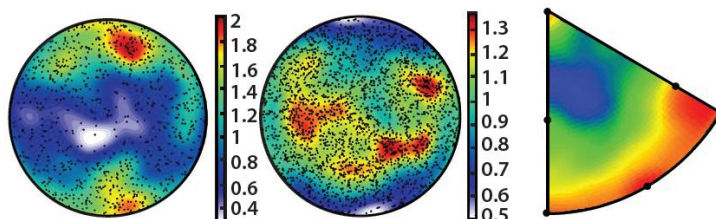
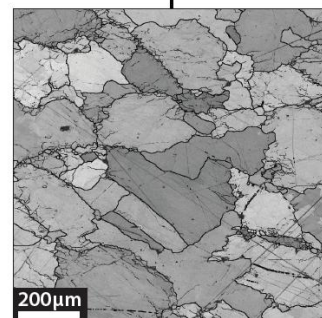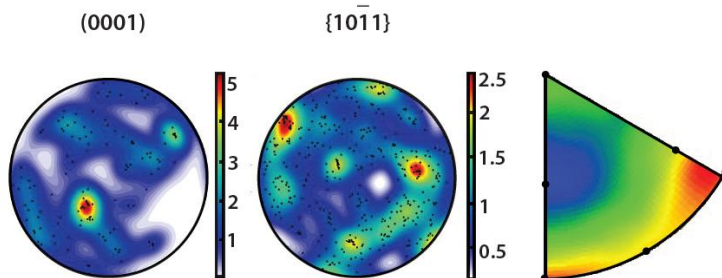**27**
PARIS: 32..98 % (L2)
$\Delta\sigma$/ T/ ε: 36 MPa /
900°C / 0.45
$\dot{\varepsilon}$: 4.5*10^{-5} s^{-1}

decreasing
flow stress

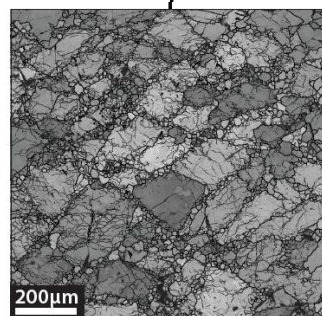(0001) {10$\bar{1}$1}
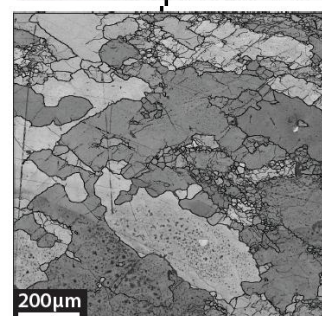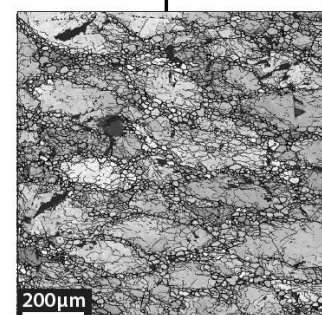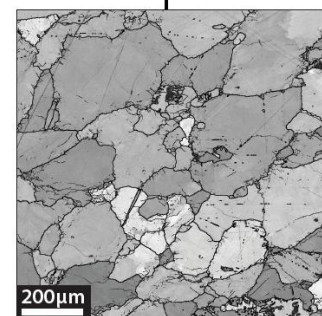
24
PARIS: 32.15 % (L2)
Δσ/ T/ ε: 36 MPa /
900°C / 0.3
ε̇: 4*10^{-5} s^{-1}

21
PARIS: 35.41 % (L2)
Δσ/ T/ ε: 36 MPa /
900°C / 0.15
ε̇: 3.7*10^{-5} s^{-1}
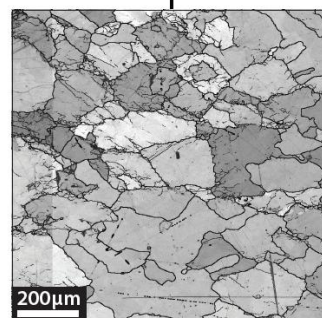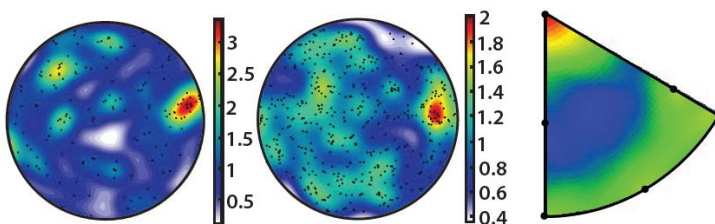
40
PARIS: 39.73 % (D)
Δσ/ T/ ε: 36 MPa /
830°C / 0.45
ε̇: 3.7*10^{-6} s^{-1}
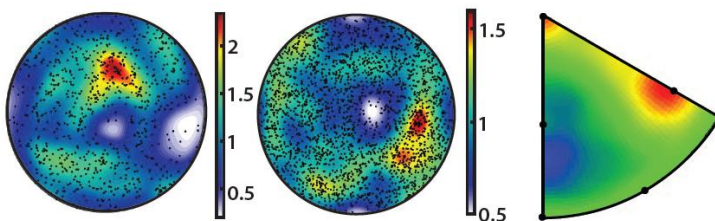
29
PARIS: 38.54 % (D)
Δσ/ T/ ε: 36 MPa /
830°C / 0.3
ε̇: 3.4*10^{-6} s^{-1}

28
PARIS: 33.43 % (L2)
Δσ/ T/ ε: 36 MPa /
830°C / 0.15
ε̇: -
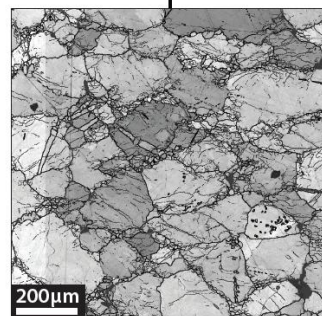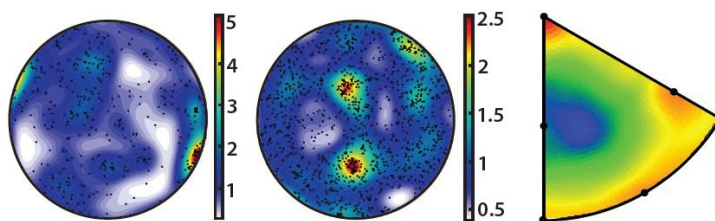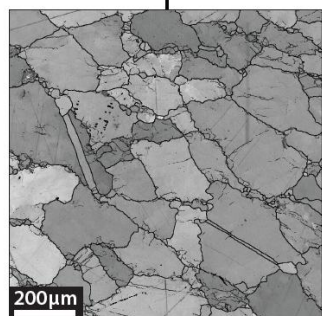
decreassing
flow stress

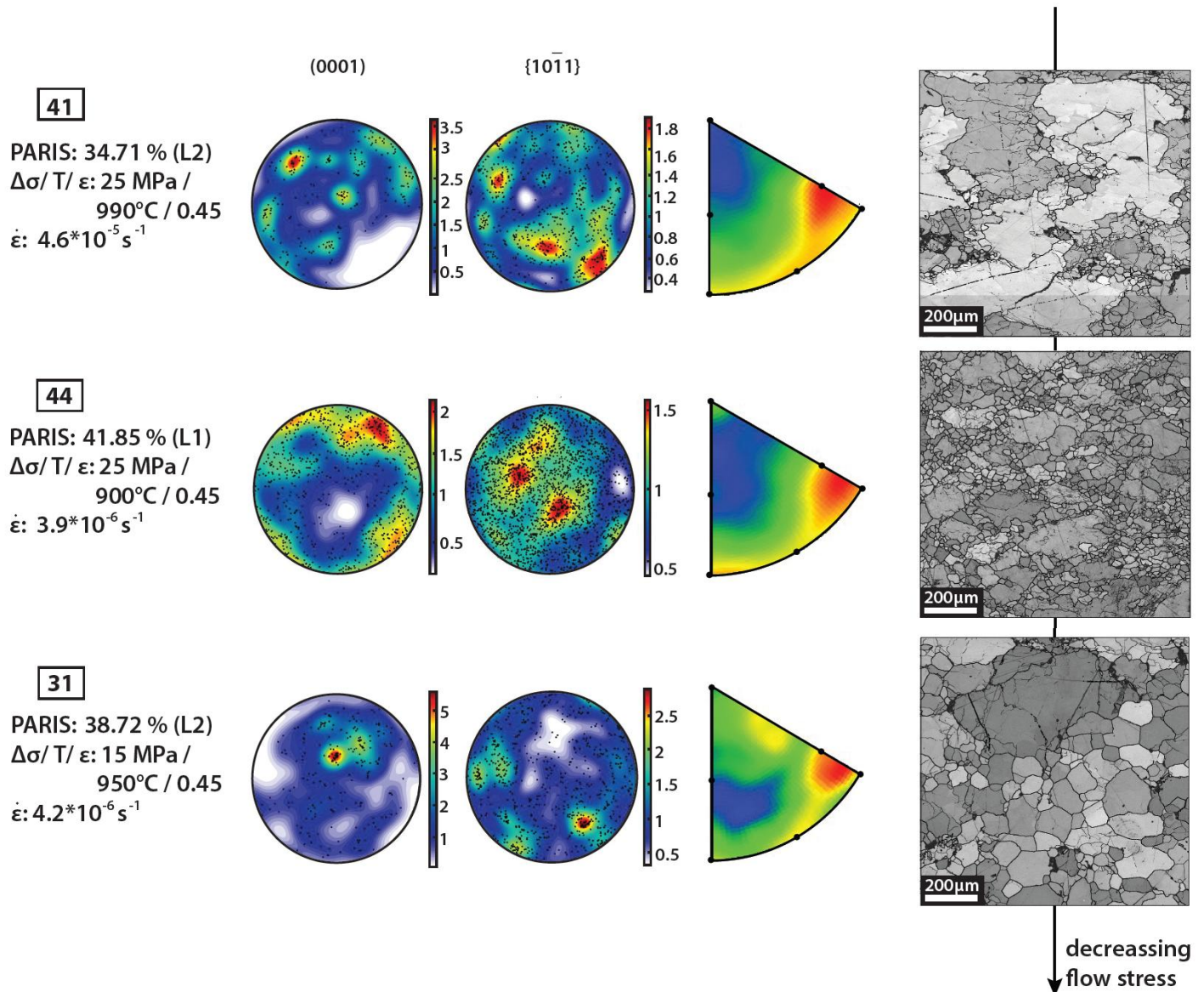**Figure 19.** Sequence of PF for c(0001) and {*f*}<10-11> planes; projections of the misorientation axis of the subgrain boundary; and grain boundary maps for: **a)** high stress, 85 to 65 MPa; **b)** medium stress, from 36 to 50 MPa; and **c)** low stress, from 15 to 25MPa. Samples have been ordered in each case by decreasing stress. It can be observed that for high stresses, there is a predominance of maxima clusters parallel to σ_1 as well as more randomly distributed PF (for $\varepsilon<0.45$). At medium stresses, CPOs can both present clusters or girdles parallel to σ_1 whereas at low stresses there is a predominance of clusters distributed randomly or weak girdles parallel to σ_1. Notice that most configurations parallel to the maxima compression direction present misorientation axis parallel to <*a*> (except for sample 35). When this last condition is not met, CPO are weaker and/or displaced to another position.

subgrains with decreasing flow stress, indicated by the m.u.d. density.

At high flow stresses, all samples have a strong misorientation axis parallel to <*a*>, and minor to {*m*} for those at 85 MPa. On the other hand, samples SV01, and 35 also present misorientation axis parallel to {*f*}, being stronger for sample 35. At medium flow stresses, all samples have a strong misorientation axis parallel to {*f*}. Sample 43 also present misorientation axis parallel to <*a*> and {*m*}. SV02 and 33 show minor parallelism to (*c*). Low flow stresses present a varied configuration, being (*c*), (*c*)+{*f*}, {*f*}+{*m*}, and <*a*>+{*f*} the predominant.

I infer that PF with [*c*]-axis maximum parallel to σ_1 contribute to the generation of misorientation axis

parallel to <a>, with edge dislocations gliding on the {f}<10-11> slip systems. Consumption of edge dislocations on {f}<10-11> can result in the transition from cluster to girdle CPO. This can be well appreciated for samples at 50 MPa, but does not occur for samples with ε < 0.45 and sample 35. Furthermore, I infer that samples that are randomly oriented present a predominance of edge and/or screw dislocations on (c)<a> and/or {f}. Based on Table 7, active dislocations would be: screw on (c), edge and screw on {f} and {m}, and edge on <a>. Nevertheless, since Ter Heege (2002) reported that the samples were controlled by dislocation-controlled cross-slip (Fig. 2) I infer that screw dislocations active on (c)<a>, and edge dislocations on {m} slip systems will not be expected. Nevertheless, Transmission Electron Microscopy (TEM) analysis should be needed to discern which kind of dislocations are present in the sample.

De Bresser and Spiers (1997) defined (c)<a> and {f}<10-11> as the most active slip systems at high temperature conditions (T>400°C) (Fig. 20), being (c)<a> the most favourable one. This is in accordance with data from Table 7 calculated from the MIPF projections (Fig. 19). My results seem to
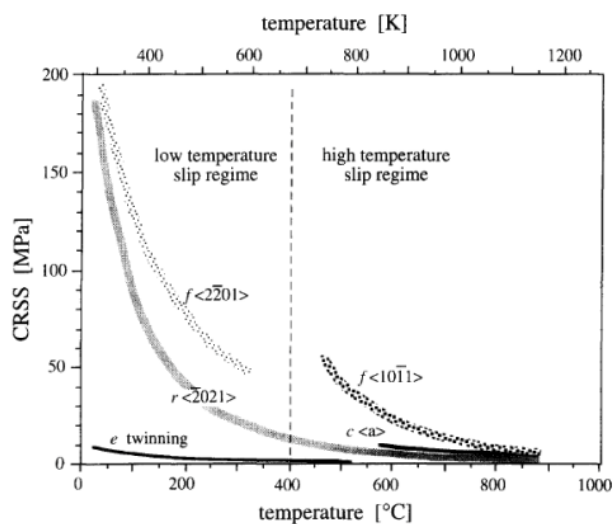

Figure 20. Plot reflecting the predominant activity of determinate slip systems at different temperatures based on the critical resolved shear stress (De Bresser and Spiers, 1997). It can be observed that for T>600°C basal and {f}<10-11> slip systems predominate.

meet De Bresser and Spiers (1997) postulation since (c)<a> direction is present on screw dislocations parallel to {f} and edge and/or screw dislocations on {m}. Furthermore, {f} slip systems seem to be active only for edge dislocations parallel to <a> and screw and/or edge dislocations on {f}. However, misorientation axis parallel to (c) are only accounted for edge dislocations perpendicular to {m} and/or screw dislocations parallel to (c). Note that {r} is not active in any sample, in accordance to De Bresser and Spiers (1997) (Fig. 20).

The projection of Schmid factors over the samples (Table 7) shows that the slip area on {f}<10-11> is higher than in (c)<a>. The probability density also indicates that at high Schmid factor values {f}>(c) for most samples, except for samples 25, 27, 34_2, 41, SV02 and SV05. Consequently, I would expect for the latter samples screw dislocations to be predominant.

4.5 Conceptual model

The model that I present is based on the idea developed by Qi *et al*. (2017) for deformation on ice. In my model (Fig. 21) I will define three different situations according to the previously presented CPOs (Fig. 19).

In the first situation PF present clear [c]-maxima clusters parallel to the compression direction. This pattern has been observed on samples SV01, 43 and 37 for diamond shaped grains and on samples 25, 34_1, and 34_2 for L1. CPO from diamond shape grains as well as 34_1 and 34_2were developed at low temperature and high differential stress whereas sample 25 CPO was developed at high temperature and low stress. In the second situation, girdles parallel to σ_1 are present instead of clusters. This pattern is observed in samples 33 and 44 for type L1, as well as in SV02 and 27 for L2. Generally this corresponds to high temperature, low differential stress conditions. I infer that the first described pole figure pattern is developed preferentially on microstructures with predominant SGR+GBS
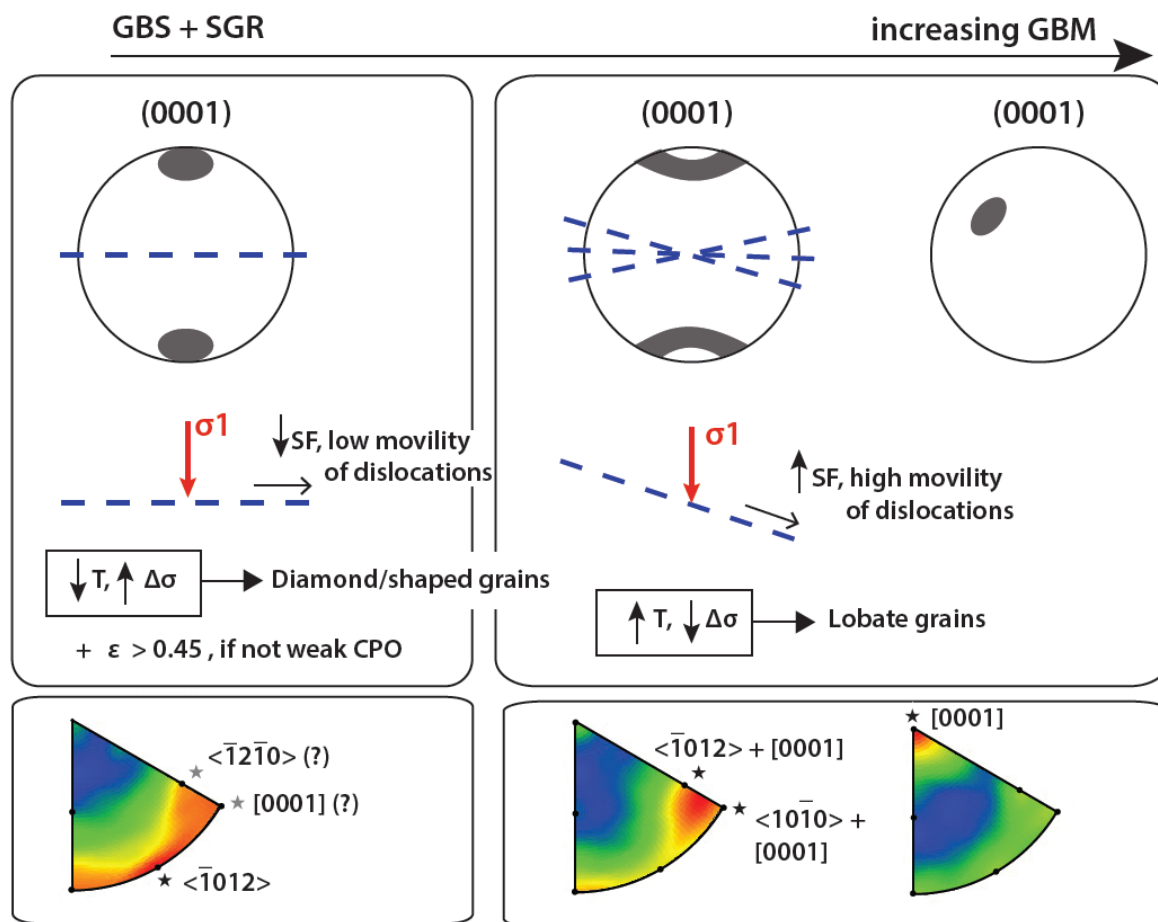
Figure 21. Model of the evolution of CPO. In the left (generally at LT-Hσ conditions), clear pole maxima parallel to σ1 are developed whereas in the right (generally at HT-Lσ conditions) CPO are weaker, forming girdles parallel to σ$_1$ and/or randomly distributed around the stereographic projection. I infer that CPOs in the left are developed due to the accumulation of dislocations in poorly-slip oriented planes (*i.e.*, low Schmid factor). Developed microstructures are generated by GBS, SGR and minor GBM. I infer a predominance of edge dislocations on the *a*{-12-10}<-2021> slip system (black star) and possible co- activity of edge dislocations at *m*{10-10}<-12-10> and *f*{-1012}<10-11> (grey stars). Weaker CPOs on the right are due to the predominance of good-slip oriented slip planes by consumption of dislocations in planes with low Schmid factors. Consumption of dislocations is generated by GBM. I infer a predominance of screw dislocations following the (*c*)<*a*> slip system.

among GBM whereas in the second case it is the opposite situation.

Furthermore, a third situation derived from the second pattern has also been observed. I refer to stronger/weaker clusters distributed along the projection in a way which is not parallel to σ$_1$. This pattern occurs preferentially in samples deformed at high temperature and low stress. Thus, I infer that they correspond to an advanced state of GBM. This kind of pattern also occurs when samples where deformed at ε<0.45. My model reflects a changing CPO on pole figures as a reflection of different dominant recrystallisation process, which in last instance impacts on the preferential slip systems

activity (Fig. 14).

When the sample is deformed a large amount of dislocations are formed within grains as a way to store elastic strain energy (Qi *et al.*, 2017). Each grain will present a different orientation with respect to the compression direction, being more (*i.e.,* plane of the grain orthogonal to σ$_1$) or less (*i.e.,* not orthogonal) favourable to dislocations to glide. For poor slip-oriented grains, dislocations will not be able to glide and thus will accumulate and tangle whereas for good slip-oriented grains dislocations will glide along the grain to the mantle (Bestmann and Prior 2003). Once at the mantles, edge dislocations will form a stacking fault (Hull

and Bacon, 1965), as described in Figure 3. This plane constitutes the misorientation axis between the planes located aside. Increasing misorientation causes SGR and if it exceeds between 10−15° it generates a recrystallised grain.

When the sample is first being deformed both grain oriented configurations are present. I infer that orthogonal configuration predominates since pole figures show a [c]-axis maximum parallel to σ_1. Furthermore, there is GBS to accommodate the strain produced by the compression, resulting in diamond-shaped grains. However, at the grain junctions strain is accumulated causing GBM with progressive SGR (Fig. 16C), triggering recrystallised grains. At higher temperature, grain boundary mobility increases and thus GBM is higher. Consequently, accumulated dislocations within poorly oriented planes for slip (*i.e.,* low Schmid factor values) are consumed. This is reflected in the PF by a change from clusters to girdles and in the microstructure by more lobate grains. If the process develops further girdles become randomly distributed, showing a weak CPO. I infer that {*f*}<10-11> slip system is most favour at LT high stress conditions, although I do not preclude the possibility of multiple slip-systems acting together (thus in agreement with the Taylor model). I also infer that dislocations within the {*f*}<10-11> slip system are progressively consumed with increasing GBM activity. For that reason basal planes become more predominant, as reported for HT conditions (Griggs *et al.*, 1960; Turner and Orozco, 1976; Schmid *et al.,*1987; De Bresser and Spiers, 1993).

The present model seems to meet the results obtained by Qi *et al*. (2017), where they reported a transition from point maxima clusters parallel to the compression direction towards girdle distributions with decreasing flow stress and where basal slip becomes more active at the same changing conditions. Nevertheless, experiments performed by Qi *et al*. (2017) did not include changing temperature conditions. My analysis illustrates that CPO evolution occurs keeping an inverse

relationship between temperature and stress. This observation is in accordance with previous documentation of microstructural evolution dominated by GBM recrystallization mechanisms with decreasing stress and increasing temperature (*e.g.,* Hirth and Tullis, 1992 for quartz). However, due to the high purity of my samples, my model does not consider the role of secondary phases and/or impurities at the grain boundaries that may affect the mobility of dislocations or transfer the stress onto second phases (Olgaard, 1990), which can be present in ice (Cyprych, *et al*., 2016)

On the other hand, Wenk *et al*. (1987) compared CPOs from natural and experimental deformed samples with (Taylor) theoretical models developed on orientation distribution function (ODF) for both pure and simple shear at low and high temperatures. Although they found a good correlation between the different samples, they reported that most natural calcite fabrics present low temperature (LT) textures and infer that {*e*} twinning had a lower prevalence in experimental deformation cases. The CPOs for pure shear consisted on maxima values for poles parallel to the compression direction forming clusters (LT texture) or girdles (HT texture). IPF-Y projections (Fig. 13) in my samples reveal a relative activity in the {*e*} direction, reflected in the microstructure with few twins on diamond-shaped grains. However, as reported previously, the amount of twins is scarce. Moreover, I have reported both LT and HT textures described by Wenk *et al*. (1987) at the same comparative conditions (but at a lower range of temperatures). Therefore, I consider that there is a good correlation between the CPOs and microstructural observations obtained in this study from those of Wenk and co-workers. Nevertheless, Wenk *et al*. (1987) did not come up to an explanation for the different CPOs, whereas I consider that evolving dynamic recrystallization mechanisms are the responsible for such textural variation.

Reported activity of GBS implies the co-presence of grain size sensitive (GSS) deformation

mechanisms in a grain size insensitive (GSI) regime. This observation has already been documented for ice (Llorens *et al.*, 2016) and olivine (Skemerand Hansen, 2015), the latter suggesting a wider range of action for GBS (Fig. 22). My results are in agreement with this last model. Furthermore, I have not reported an increase of average misorientation between recrystallized grains, randomisation nor CPO strength weakening due to GBS, as suggested by Bestmann and Prior (2003).

Finally, I consider that the presented model does not work for static recrystallization. On one hand, Boneh *et al.* (2017) performed static annealing studies on experimentally deformed olivine, where they found discontinuous-growth of grains. Changing grain size distribution and dislocation density was based on different duration of static annealing. Therefore, Boneh and co-workers argued that small dislocation-free grains experienced a rapid grain growth at expenses of the surrounding high-dislocation grains (matrix), which kept without growing due to the presence of a previous strong CPO. On their work, they excluded the possibility of inhabitation of the matrix growth by presence of impurities at grain boundaries or the effect of pinning by secondary phases at the grain boundaries. On the other hand, Heilbronner and Tullis (2002) performed static annealing studies on quartzite samples, with continuous-growth of grains. The CPO kept their original distribution but decreased on strength. However, Green (1967) found an increase of CPO strength. There is still not a consensus regarding the impact of annealing on CPO. In my opinion, since the nature of the recrystallization mechanisms between our experiments is different, I consider that we cannot compare both models. Nevertheless, it would be interesting for further studies to link both processes. Besides, both their results and mine reveal that dynamic/static recrystallization may infer on the original paleostress indicators and alter the anisotropical properties of the rock. This should be taken into account for instance when studying the original conditions at which rocks were deformed or for seismic modelling.
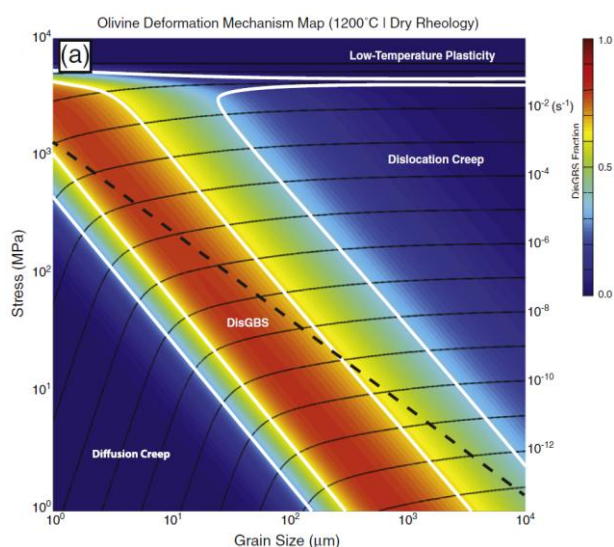

Figure 22. GBS domain on a deformation map for olivine. The plot was calculated by using the flow law for dislocation and diffusion creep. It can be observed that the contribution of GBS domain is wide and not only limits to diffusion creep (Skemer and Hansen, 2015).

5. CONCLUSIONS

1. Changing activity on recrystallisation mechanisms can be reflected on changing CPO patterns.

2. At low T and high flow stresses pole figures present [*c*]-axis maximus parallel to σ_1, indicating poorly slip-oriented grains (*i.e.*, low Schmid factor). GBS is the main deformation process and dominant recrystallisation mechanisms are SGR with minor GBM. Grains present angular/diamond-shape morphologies.

3. At high T and low flow stresses pole figures present girdles parallel to σ_1, indicating good slip-oriented grains (*i.e.*, high Schmid factor); or randomly distributed clusters. Dominant recrystallisation mechanism is GBM. Grains present lobate shape morphologies.

4. Edge dislocations on the {*f*}<10-11> slip system seem to be predominant at low T and high flow stresses.

5. Increasing GBM activity consumes dislocations on the {*f*}<10-11> slip system, leaving dislocations on the basal slip system.

6. PARIS factor has shown to be not adequate as grain shape indicator to differentiate lobate from diamond shape grains.

7. Separated analysis of porphyroclast and recrystallised fractions indicate same results as the analysis of both together.

REFERENCES

Barnhoorn, A., 2003. Rheological and microstructural evolution of carbonate rocks during large strain torsion experiments. PhD. ETH Zürich, 146pp.

Barth, N.C., Hacker, B.R., Seward, G.G.E., Walsh, E.O., Young, D., Johnston, S., 2010. Strain within the ultrahigh pressure Western Gneiss region of Norway recorded by quartz CPO. In: Law, R.D., Butler, R.W.H., Holdsworth, R.E., Krabbendam, M., Strachan, R.A. (eds.). Continental Tectonics and Mountain Building: The Legacy of Peach and Horne. Geological Society, London, Special Publications, 335, 663−685.

Berhrmann, J.H., Platt, J.P., 1982. Sense of nappe emplacement from quartz c-axis fabrics: an example from the Betic Cordilleras (Spain). Earth and Planetary Science Letters, 59, 208−215.

Bestmann, M., Prior, D.J., 2003. Intragranular dynamic recrystallisation in naturally deformed calcite marble: diffusion accommodated grain boundary sliding as a result of subgrain rotation recrystallisation. Journal of Structural Geology, 25, 1597–1613.

Bestmann, M., Kunze, K., Matthews, A., 2000. Evolution of a calcite marble shear zone complex on Thassos Island, Greece: microstructural and textural fabrics and their kinematic significance. Journal of Structural Geology, 22, 1789–1807.

Boneh, Y., Wallis, D., Hansen, L.N., Krawczynski, M.J., Skemer, P., 2017. Oriented grain growth and modification of "frozen anisotropy" in the lithospheric mantle. Earth and Planetary Science Letters, 474, 368−374.

Bunge, H.J., 1982. Texture analysis in material science. Mathematical Methods. Cuvillier Verlag, Göttingen, 308pp.

Burlini, L., Marquer, D., Challandes, N., Mazzola, S., Zangarini, N., 1998. Seismic properties of highly strained marbles from the Splügenpass, central Alps. Journal of Structural Geology, 20(2), 277−292.

Cao, W.W., Godfrey, A., Liu, Q., 2003. Determining dislocation cell sizes for high-strain deformation microstructures using the EBSP technique. Journal of microscopy, 211, 219−229.

Castelnau, O., Blackman, D.K., Becker, T.W., 2009. Numerical simulations of texture development and associated rheological anisotropy in regions of complex mantle flow. Geophysical Research Letters, 36, L12304.

Cornelius, S.H., Cornelis, K., 1997. Manual de mineralogía: basado en la obra de J.D. Dana. Reverte, 396pp.

Cossette, E., Schneider, D., Audet, P., Grasemann, B., Habler, G., 2015. Seismic properties and mineral crystallographic preferred orientations from EBSD data: Results from a crustal-scale detachment system, Aegean region. Tectonophysics, 651-652, 66−78.

Covey-Crump, S.J., 1998. Evolution of mechanical state in Carrara marble during deformation at 400° to 700°C. Journal of Geophysical Research, 103, 29781−29794.

Cyprych, D., Piazolo, S., Wilson, C.J.L., Luzin, V., Prior, D.J., 2016. Rheology, microstructure and crystallographic preferred orientation of matrix containing a dispersed second phase: insight from experimentally deformed ice. Earth and Planetary Science Letters, 449, 272−281.

De Bresser, J.H.P., 1991. Intracrystalline deformation of calcite. PhD. Utrecht University, 203pp.

De Bresser, J.H.P., 2002. On the mechanism of dislocation creep of calcite at high temperature: Inferences from experimentally measured pressure sensitivity and strain rate sensitivity of flow stress. Journal of Geophysical Research, 107(B12), 2337−2353.

De Bresser, J.H.P., Spiers, C.J., 1993. Slip Systems in calcite single crystals deformed at 300-800°C. Journal of Geophysical Research, 98(B4), 6397−6409.

De Bresser, J.H.P., Spiers, C.J., 1997. High-temperature deformation of calcite single crystals by r+ and f+

slip. In: Knipe, R.J., Rutter, E.H. (eds.). Deformation Mechanisms, Rheology and Tectonics, Geological Society Special Publication, 54, 285−298.

Deer, W.A., Howie, R.A., Zussman, J., 1962. Rock-forming minerals-Vol 5, non-silicates. Longmans, Green and co Ltd., 301pp.

Drury, M.R., Humphreys, F.J., 1988. Microstructural shear criteria associated with grain-boundary sliding during ductile deformation. Journal of structural Geology, 10(1), 83−89.

Drury, M.R., Humphreys, F.J., White, S.H., 1989. Effect of dynamic recrystallisation on the importance of grain-boundary sliding during creep. Journal of materials science, 24, 154−162.

Drury, M.R., Urai, J.L., 1989. Deformation-related recrystallisation processes. Tectonophysiscs, 172, 235−253.

Frost, H.J., Ashby, M.F., 1982. Deformation Mechanism Maps. The plasticity and creep of metals and ceramics. Pergamon Press, Oxford, 166pp.

Gifkins, R.C., 1976. Grain boundary sliding and its accommodation during creep and superplasticity. Metallurgical Transactions, A7, 1225−1232.

Green, H., 1967. Quartz: extreme preferred orientation produced by annealing. Science, 157, 1444−1447.

Griggs, D.T., 1936. Deformation of rocks under high confining pressures-I. Experiments at room temperature. Journal of Geology, 44, 541−577.

Griggs, D.T., Turner, F.J., Heard, H.C., 1960. Deformation of rocks at 500 to 800°C. Geological Society of the American Memoir, 79, 39−105.

Hansen, L.N., Zimmerman, M.E., Kohlstedt, D.L., 2011. Grain boundary sliding in San Carlos olivine: Flow law parameters and crystallographic-preferred orientation. Journal of Geophysical Research, 116, B09201.

Hansen, L.N., Zhao, Y., Zimmerman, M.E., Kohlstedt, D.L., 2014. Protracted fabric evolution in olivine:

Implications for the relationship among strain, crystallographic fabric, and seismic anisotropy. Earth and Planetary Science Letters, 387, 157−168.

Hansen, L.N., Warren, J.M., Zimmerman, M.E., Kohlstedt, D.L., 2016a. Viscous anisotropy of textured aggregates, Part 1: Measurement of the magnitude and evolution of anisotropy. Earth and Planetary Science Letters, 445, 92−103.

Hansen, L.N., Conrad, C.P., Boneh, Y., Skemer, P., Warren, J.M., Kohlstedt, D.L., 2016b. Viscous anisotropy of textured aggregates, Part 2: Micromechanical model. Journal of Geophysical Research: Solid Earth, 121, 7137−7160.

Heilbronner, R., Barrett, S., 2014. Image Analysis in Earth Sciences. Microstructures and Textures of Earth Materials. Springer, Berlin. 520pp.

Hirth, G., Tullis, J., 1992. Dislocation creep regimes in quartz aggregates. Journal of Structural Geology, 14(2), 145−159.

Hull, D., Bacon, D.J., 1965. Introduction to dislocations. Elsevier, Oxford, 268pp.

Kocks, U.F., Tomé, C.N., Wenk, H.R., 2000. Texture and anisotropy: preferred orientations in polycrystals and their effect on materials properties. Cambridge University Press, 668pp.

Llorens, M.G., Griera, A., Bons, P.D., Roessiger, J., Lebensohn, R., Evans, L., Weikusat, I., 2016. Dynamic recrystallization of ice aggregates during co-axial viscoplastic deformation: a numerical approach. Journal of glaciology, 232, 359−377.

McKie, D., McKie, C., 1986. Essentials of crystallography. Blackwell Scientific Publications, 437pp.

Molli, G., Conti, P., Giorgetti, G., Meccheri, M., Oesterling, N., 2000. Microfabric study on the deformational and thermal history of the Alpi Apuane marbles (Carrara marbles), Italy. Journal of Structural Geology, 22, 1808−1825.

Mügge, O., 1883. Beiträge zur Kenntnis der Strukturflächen des Kalkspaths. Neues Jahrbuch

für Mineralogie, 1, 32−54, 81−85.

Olgaard, D.L., 1990. The role of second phase in localizing deformation. In: Knipe, R.J., Rutter, E.H. (eds.). Deformation Mechanisms, Rheology and Tectonics, Geological Society Special Publication, 54, 175−181.

Orowan, E., 1934. Plasticity of crystals. Zeitschrift fur Physik, 89, 605−659

Panozzo, R., Hürhmann, H., 1983. A simple method for the quantitative discrimination of convex and convex-concave lines. Microscopica Acta, 87, 169−176.

Passchier, C.W., Trouw, R.A.J., 2005. Microtectonics. Springer, Berlin. 366pp.

Paterson, M.S., Turner, F.J., 1970. Experimental deformation of constrained crystals of calcite in extension. In: Paulitsch, P. (ed.). Experimental and natural rock deformation. Proceedings International Symposium, Darmstadt February 1969. Springer Verlag, 109−141.

Peternell, M., Hasalová, P., Wilson, C.J.L., Piazolo, S., Schulmann, K., 2010. Evaluating quartz crystallographic preferred orientations and the role of deformation partitioning using EBSD and fabric analyser techniques. Journal of Structural Geology, 32, 803−817.

Phillips, F.C., 1962. An introduction to crystallography. Longmans, Green and Co Ltd., 340pp.

Pieri, M., Burlini, L., Kunze, K., Olgaard, D.L., Stretton, I.C., 2001. Rheological and microstructural evolution of Carrara marble with high shear strain: results from high temperature torsion experiments. Journal of Structural Geology, 23, 1393−1413.

Polanyi, M., 1934. Lattice distortion which originates plastic flow. Zeitschrift fur Physik, 89, 660.

Qi, C., Goldsby, D.L., Prior, D.J., 2017. The down-stress transition from cluster to cone fabrics in experimentally deformed ice. Earth and Planetary Science Letters, 471, 136−147.

Renner, J., Evans, B., Siddiqi, G., 2002. Dislocation

creep of calcite. Journal of Geophysical Research, 107(B12), 2364.

Rhines, F.N., Bond, W.E., Kissel, M.A., 1956. Grain boundary creep in aluminium bicrystal. Transactions of American Society for Metals, 48, 919−951.

Rutter, E.H., 1974. The influence of temperature, strain-rate and interstitial water in the experimental deformation of calcite rocks. Tectonophysics, 22, 311−334.

Rutter, E.H., 1995. Experimental study of the influence of stress, temperature and strain on the dynamic recrystallisation of Carrara marble. Journal of Geophysical Research, 100, 24651−24663.

Rutter, E.H., Casey, M., Burlini, L., 1994. Preferred crystallographic orientation development during the plastic and superplastic flow of calcite rocks. Journal of Structural Geology, 16 (10), 1431−1446.

Sachs, G., 1928. Zur Ableitungeiner Fließbedingung. Z. Ver. Deu. Ing., 72(22), 734−736.

Scheidegger, A.E., 1965. On the statistics of the orientation of bedding planes, grain axes and similar sedimentological data. United States Geological Survey Professional Paper, 525(C), C164−C167.

Schmid, S.M., Paterson, M.S., Boland, J.N., 1980. High temperature flow and dynamic recrystallisation in Carrara marble. Tectonophysics, 65, 245−280.

Schmid, S.M., Panozzo, R., Bauer, S., 1987. Simple shear experiments on calcite rocks: rheology and microfabric. Journal of Structural Geology, 9, 747−778.

Skemer, P., Hansen, L.N., 2015. Inferring upper-mantle flow from seismic anisotropy: An experimental perspective. Tectonophysics, 668−669, 1−14.

Skemer, P., Katayama, I., Jiang, Z., Karato, S., 2005. The misorientation index: Development of a new method for calculating the strength of lattice - preferred orientation. Tectonophysics, 411, 157−167.

Skemer, P., Warren, J.M., Hirth, G., 2012. The influence of deformation history on the interpretation of seismic anisotropy. Geochemistry, Geophysics,

Geosystems, 13(3), Q03006.

Smith, S.A.F., Billi, A., Di Toro, G., Spiess, R., 2011. Principal slip zones in limestone: microstructural characterization and implications for the seismic cycle (Tre Monti Fault, Central Apennines, Italy). Pure and Applied Geophysics, 168, 2365−2393.

Speight, M.V., 1976. The role of grain-boundary sliding in the creep of polycrystals. Acta metallurgica, 24, 725−729.

Taylor, G.I., 1934. The mechanism of plastic deformation of crystals. Proceedings of the Royal Society of London, 145,362−404.

Ter Heege, J.H., 2002. Relationship between dynamic recrystallisation, grain size distribution and rheology. PhD. Utrecht University, 141pp.

Thomas, J.M., Renshaw, G.D., 1967. Influence of dislocations on the thermal decomposition of calcium carbonate. Journal of the Chemical Society, A, 2058−2061.

Turner, F.J., Heard, H.C., 1965a. Deformation in calcite crystals at different strain rates. University of California Publications on Geological Sciences, 46, 103−126.

Turner, F.J., Orozco, M., 1976. Crystal bending in metamorphic calcite, and its relations to associated twinning. Contributions to Mineralogy and Petrology, 57, 83−97.

Valcke, S.L.A., 2008. EBSD analysis of heterogeneous microstructures in experimentally deformed calcite: development of core and mantle subgrains, grain boundary bulges and recrystallised grains. PhD. University of Utrecht, 143pp.

Vollmer, F.W., 1990. An application of eigenvalue methods to structural domain analysis. Geological Survey of American Bulletin, 102, 786−791.

Walker, A.N., Rutter, E.H., Brodie, K.H., 1990. Experimental study of grain-size sensitive flow of synthetic, hot-pressed calcite rocks. In: Knipe, R.J., Rutter, E.H. (eds.). Deformation Mechanisms, Rheology and Tectonics. Geological Society Special Publication, 54, 259−284.

Wallis, D., Hansen, L.N., Britton, T.B., Wilkinson, A.J., 2017. Dislocation interactions in olivine revealed by HR-EBSD. Journal of Geophysical Research: Solid Earth, 122.

Wallis, D., Lloyd, G.E., Hansen, L.N., 2018. The role of strain hardening in the transition from dislocation-mediated to frictional deformation of marbles within the Karakoram Fault Zone, NW India. Journal of Structural Geology, 107, 25−37.

Watson, G.S., 1966. The statistics of orientation data. Journal of Geology, 74, 786−797.

Weikusat, I., Kuiper, E.N., Pennock, G.M., Kipfstuhl, S., Drury, M.R., 2017. EBSD analysis of subgrain boundaries and dislocation slip systems in Antartic and Greenland ice. Solid Earth, 8, 883−898.

Wenk, H.R., Takeshita, T., Bechler, E., Erskine, B.G., Matthies, S., 1987. Pure shear and simple shear calcite textures. Comparison of experimental, theoretical and natural data. Journal of Structural Geology, 9(5-6), 731−745.

Wenk, H.R., Christie, J.M., 1991. Review Paper. Comments on the interpretation of deformation textures in rocks. Journal of Structural Geology, 13(10), 1091−1110.

Wenk, H.R., 2002. Texture and anisotropy. In: Karato, S.I., Wenk, H.R. (eds.). Plastic deformation of minerals and rocks. Reviews in Mineralogy and Geochemistry, Mineralogical Society of America and Geochemical Society, Washington, DC, 51, 291−329.

Wheeler, J., Prior, D., Jiang, Z., Spiess, R., Trimby, P., 2001. The petrological significance of misorientations between grains. Contributions to Mineralogy and Petrology, 141, 109−124.

Woodcock, N.H., 1977. Specification of fabric shapes using an eigenvalue method. Geological Society of American Bulletin, 88, 1231−1236.

Zhang, S., Karato, S., 1995. Lattice preferred orientation of olivine aggregates deformed in simple shear. Nature, 375, 7741−777.